VoxCity: A Seamless Framework for Open Geospatial Data Integration, Grid-Based Semantic 3D City Model Generation, and Urban Environment Simulation

Kunihiko Fujiwara[a,b], Ryuta Tsurumi[c], Tomoki Kiyono[d], Zicheng Fan[a], Xiucheng Liang[a], Binyu Lei[a], Winston Yap[a], Koichi Ito[a], Filip Biljecki[a,e,*]

[a]*Department of Architecture, National University of Singapore, 4 Architecture Drive, 117566, Singapore*
[b]*Research & Development Institute, Takenaka Corporation, 1-5-1 Otsuka, Inzai, Chiba, 270-1352, Japan*
[c]*Nikken Sekkei Research Institute, 3-7-1 Kanda Ogawamachi, Chiyoda-ku, Tokyo, 101-0052, Japan*
[d]*Institute of Urban Innovation, Yokohama National University, 79-5 Tokiwadai, Hodogaya, Yokohama, Kanagawa, 240-8501, Japan*
[e]*Department of Real Estate, National University of Singapore, Singapore*

Abstract

Three-dimensional urban environment simulation is a powerful tool for informed urban planning. However, the intensive manual effort required to prepare input 3D city models has hindered its widespread adoption. To address this challenge, we present VoxCity, an open-source Python package that provides a one-stop solution for grid-based 3D city model generation and urban environment simulation for cities worldwide. VoxCity's 'generator' subpackage automatically downloads building heights, tree canopy heights, land cover, and terrain elevation within a specified target area, and voxelizes buildings, trees, land cover, and terrain to generate an integrated voxel city model. The 'simulator' subpackage enables users to conduct environmental simulations, including solar radiation and view index analyses. Users can export the generated models using several file formats compatible with external software, such as ENVI-met (INX), Blender, and Rhino (OBJ). We generated 3D city models for eight global cities, and demonstrated the calculation of solar irradiance, sky view index, and green view index. We also showcased microclimate simulation and 3D rendering visualization through ENVI-met and Rhino, respectively, through the file export function. Additionally, we reviewed openly available geospatial data to create guidelines to help users choose appropriate data sources depending on their target areas and purposes. VoxCity can significantly reduce the effort and time required for 3D city model preparation and promote the utilization of urban environment simulations. This contributes to more informed urban and architectural design that considers environmental impacts, and in turn, fosters sustainable and livable cities. VoxCity is released openly at https://github.com/kunifujiwara/VoxCity.

Keywords: Urban morphology, Digital Twin, Thermal environment, Ray-tracing, Thermal comfort, Built environment, View factor

1. Introduction

Three-dimensional urban environment simulations facilitate assessing various conditions including outdoor heat stress [1, 2], wind flow [3], visual perception [4, 5], building energy demand [6, 7], air quality [8], and noise propagation [9, 10], at high spatial and temporal resolution. Their results help diverse applications including policy-making, urban planning, city management, architectural and landscape design [11, 12, 13]. Such urban environment simulations require 3D city models with semantic information for diverse elements. For example, microclimate simulation uses heat-related parameters such as heat conductivity, solar reflectance, transmittance, and evaporation coefficients for each object [14, 15]. Therefore, models need to define semantic

*Corresponding author. Email: filip@nus.edu.sg

classes of objects, such as buildings, roads, vegetation, and water bodies, that determine these parameters. Simulation of visual perception also requires similar semantic information to evaluate visibility of greenery or buildings [16, 17, 18]. However, in most cases of urban environment simulations, researchers and engineers must prepare such 3D city models themselves due to a lack of available data sources [19, 20]. The intensive manual effort required to create or adapt these models has been a significant bottleneck for urban environment simulations. Although some cities have prepared open 3D city models with semantic attributes, the coverage of such data is currently limited. Moreover, existing models may not be simulation-ready because of issues such as incompatible data formats, unsealed solid geometries, and insufficient semantic information [3, 21, 19].

Meanwhile, an increasing amount of global geospatial data relevant to 3D city models has been openly released in the last few years, largely due to rapid advancements in deep learning techniques [22, 23, 24, 25]. For instance, Sirko et al. [26] released building height data with a 4 m spatial resolution for Africa, South Asia, Southeast Asia, Latin America and the Caribbean; Tolan et al. [23] published global canopy height data at a 1 m resolution; Zanaga et al. [24] released land cover data with worldwide coverage at a 10 m resolution; and Hawker et al. [25] created global terrain elevation data with a 1 Arc-second (30.9 m at the equator) resolution, based on Copernicus DEM, canopy height and building footprint data. We can use these open geospatial datasets to create 3D city models with semantic information regarding buildings, trees, land cover, and terrain. However, while these datasets can reduce the efforts required to collect necessary information and increase the coverage, they still require intensive manual efforts to integrate them and reconstruct 3D city models of sufficient quality for advanced uses such as simulations. Each dataset has different data types, such as raster and vector, and varying spatial resolutions, making the data integration process complex. To scale applications of urban environment simulation globally, it is desirable to automate these manual efforts for data integration. Moreover, even with simulation-ready models, working in simulation software remains time-consuming, particularly for tasks such as data import, boundary condition settings, and result data export.

Several open-source packages have been developed to address these challenges. 3dfier [27] and City4CFD [21, 3] automate the integration of land use and point cloud data to generate semantic 3D city models. They enable users to prepare input 3D city models for urban environmental simulations; however, point cloud data is not available for most cities, and they do not incorporate tree canopies. UMEP [28] offers functionality to simulate urban thermal and wind environments using 3D city models; however, users need to prepare input datasets including building digital surface models (DSMs) and vegetation DSMs, which require manual efforts, and are, moreover, not available for most cities. Additionally, to the best of our knowledge, there are no open packages that provide seamless functionality encompassing open geospatial data integration, 3D city model generation, and urban environment simulation.

To bridge the gap between 3D model generation and urban environment simulation, a meshing process fundamentally needs to be incorporated. Many urban environment simulation methods include the process where 3D city models are split into meshes with certain scales. For example, Computational Fluid Dynamics (CFD) for wind environment simulation requires volume meshes for fluid (air) domains and surface meshes for solid objects, such as buildings and ground [29]. Ray-tracing for solar irradiance simulation requires surface meshes of solid objects, where solar radiation is reflected or absorbed [30]. There are two principal methods for the meshing process: structured meshing and unstructured meshing. Structured meshing is a grid-based approach to create cuboid volume meshes and rectangular surface meshes [31, 32]. Unstructured meshing does not rely on a grid and generates polyhedral volume meshes and triangular surface meshes, allowing for more flexibility in shape and proportion [33, 29]. Numerous software packages employ structured meshing due to its lower computational load for both calculation and memory, as well as its stability in numerical simulations. Unstructured meshing has the advantage of incorporating curved surfaces; however, it can generate low-quality meshes with overly sharp or blunt vertex angles, leading to divergence or low accuracy in numerical simulations. For city-scale applications, structured meshing should be more desirable than unstructured meshing. More specifically, the voxel-based approach, which applies the same mesh size for the entire domain in structured meshing[34, 35, 36], offers advantages in simplicity, as a single 3D array and a specified

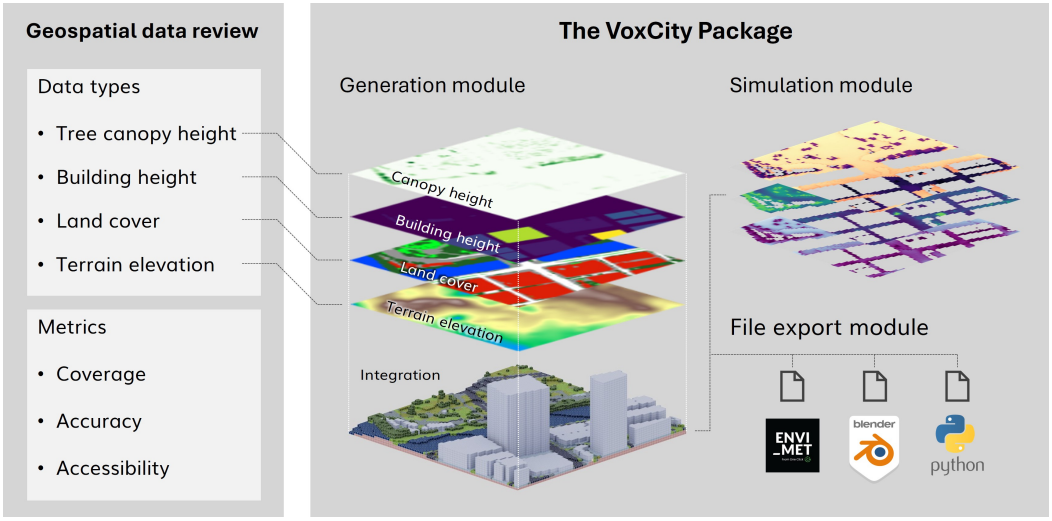

Figure 1: Framework of the development of VoxCity.

voxel size can represent the entire mesh. Moreover, voxels have better compatibility with raster formats that are commonly used in geospatial data, such as land cover, tree canopy height, and terrain elevation.

Therefore, this paper introduces 'VoxCity', an open-source Python package that provides a seamless solution for voxel-based geospatial data integration, 3D city model generation, and urban environment simulation. The framework is illustrated in Figure 1. We review open geospatial data, including building height, tree canopy height, land cover, and terrain elevation data types, and select appropriate data sources for our 3D city model generator based on metrics such as coverage, accuracy, format and accessibility. VoxCity automates the process of downloading, voxelizing, and integrating geospatial data from the selected sources to generate voxel-based 3D city models with semantic information. The package includes a subpackage for urban environment simulation, providing users an end-to-end workflow from data acquisition and integration through model generation and simulation. Furthermore, VoxCity supports multiple export file formats, ensuring compatibility with various external 3D modeling and simulation software packages.

2. Background and Related Work

2.1. Urban Environment Simulation

Climate change [37] has intensified heat-related challenges like frequent heat waves [38, 39] and urban heat island effects [40], spurring increased assessment of outdoor heat stress and thermal comfort through CFD [41, 2], radiation transfer models [1, 42, 43], and heat conduction and energy balance analyses [44]. The objectives of microclimate simulations have encompassed not only heat-related health issues but also other diverse aspects such as energy consumption for heating, ventilation, air conditioning (HVAC), and lighting [6, 7, 45, 46], air quality [47, 48], wind comfort [49, 50], wind pressure on building surfaces [51, 52], and sunlight and ultraviolet exposure focusing on human skin health [53]. Additionally, numerous studies have reported impacts of buildings [54, 55, 56, 57], trees [58, 59, 60, 61, 62], low vegetation [63, 64, 65], water bodies [66, 67, 68], and terrain morphology [69] on the microclimate, indicating the importance of including these urban elements in 3D city models for simulations.

Meanwhile, many studies have conducted urban environment simulations to assess the visual comfort of streetscapes [5] and window views [70, 71]. Specifically, sky view factor (SVF) or sky view index (SVI) [72] and green view index (GVI) [73, 71, 74] have mainly been evaluated as quantitative indicators using 3D city models with buildings, trees, and low vegetation land covers. Numerous studies have employed street view imagery and computer vision techniques instead of simulations with 3D city models to evaluate view indices [75, 76, 77, 78, 79]. This enables view analyses without preparing detailed 3D city models; however, such analyses cover only

viewpoints along street networks, and furthermore, not all streets have sufficient imagery. These view indicators have been assessed focusing not only on visual comfort but also on walkability [80, 76] and bikeability [81] of streets, the well-being of city dwellers [82], and the preferences of residents and real-estate prices [83, 84]. The visibility of water features, including the ocean, lakes, and rivers, has also been discussed in the same context [85].

Table A.7 in Appendix illustrates the relationships between simulation categories and the urban elements incorporated into 3D city models used in previous studies. Our literature review revealed that buildings, trees, land cover, water bodies, and terrain elevation have been included as essential information in 3D city models across different simulation objectives.

2.2. Creation of 3D city models

Numerous studies have prepared their 3D city models by processing point clouds acquired through LiDAR measurements [42, 86, 87, 27], or by processing polygon data acquired through photogrammetry methods [88]. While these methods can reduce the manual effort required for 3D city model preparation, their input data—point cloud data from LiDAR or multi-view photography—is not readily available in most cases.

Meanwhile, an increasing number of studies have employed open 3D city models that have been individually released by countries or cities [89, 90, 91, 92, 93]. However, in most cases, we still need to create 3D city models ourselves because cities with such available models are limited [19]. Furthermore, the data, even when openly available, is not always directly compatible with urban environment simulations. For instance, while 3D city models fundamentally include building data, only a portion of them have other semantic information, including trees and land cover [20]. Many software solutions for urban environment simulation require their own input file formats for 3D city models, such as the ENVI-met[1] geometry file (INX) and the ANSYS[2] mesh file (MSH). Additionally, some simulations require geometrically complete models for their meshing processes. Software for CFD simulations tends to require precise watertight geometries for solid objects and does not accept polygons with gaps and intersections [3, 21]. Therefore, even for studies targeting areas with open 3D city models, many of them need to add missing information from other data sources, convert file formats, or modify them to meet quality standards.

Our review of the preparation of 3D city models highlights the significant lack of available 3D city models with sufficient quality for urban environment simulations, while there is a strong demand for methods to generate 3D city models from openly available data sources for many cities.

2.3. Related work

There are several open-source tools to generate 3D city models. For instance, 3dfier [27] is an open-source software to generate 3D building models from point cloud data and building footprints. BlenderGIS[3] is a plug-in tool for Blender[4], a free and open-source 3D modeling software, which generates 3D city models by combining building data from OpenStreetMap[5] and terrain elevation from Shuttle Radar Topography Mission (SRTM) [94]. However, we were unable to find any open-source tools that could generate 3D city models containing all essential elements and attributes, including buildings, vegetation, water bodies, and terrain.

Several previous studies suggest a potential solution to the demand for a semantic 3D city model generator. Ding et al. [95] and Li and Wang [43] integrated multiple geospatial data to create 3D city models with semantic information and conducted microclimate simulations using the generated models. Specifically, Ding et al. [95] combined data on building height, land cover, and terrain elevation, while Li and Wang [43] combined building height and tree canopy height. Although Ding et al. [95] and Li and Wang [43] created land cover data using aerial imagery and building data using aerial LiDAR data respectively, they directly used openly available data sources for other data types. If these methods can be extended to encompass all essential data

[1] `https://envi-met.com/`
[2] `https://www.ansys.com/`
[3] `https://blender-addons.org/blendergis-addon/`
[4] `https://www.blender.org/`
[5] `https://www.openstreetmap.org`

types—building height, land cover, canopy height, and terrain elevation—and if all these data can be collected from openly and globally available data sources, such a tool would be highly beneficial for many researchers and engineers working on urban environment simulations.

Existing open datasets vary considerably in their spatial coverage, accuracy, and resolutions. Despite the importance of these factors for application in 3D city modeling and urban environment simulation, we were unable to find any studies offering a systematic comparison for such datasets. This gap underscores the importance of cataloging available open geospatial data, and evaluating their quality and applicability in generating semantic 3D city models. However, no studies have reviewed open geospatial data from this perspective.

Meanwhile, an increasing number of studies have proposed open-source tools as Python packages [27, 96, 97, 98, 99, 100]. For example, Yap et al. [96] introduced the Python package 'Urbanity' to automate the construction of feature-rich urban networks at any geographical scale and any location. Gholami et al. [97] developed a Python-based approach to assess microscale human thermal stress in urban environments. Python is one of the most dominant programming languages for data science, especially in machine learning. Many Python users openly share their scripts and packages through platforms such as GitHub[6] and PyPI[7], facilitating easier and more scalable distribution of developed tools.

Therefore, we propose a tool that offers two key contributions: reducing the manual effort required to prepare 3D city models for urban environment simulations, and enabling broader applications of these simulations in environmental research and urban-architectural design projects. To achieve these contributions, we present three main developments:

1. Review of open geospatial data. We review publicly available geospatial datasets—including building height, tree canopy height, land cover, and terrain elevation—focusing on crucial metrics for 3D city modeling, such as coverage, spatial resolutions, and accuracy. We identify suitable data sources for the 3D city model generation process and compile them into a comprehensive catalog. This catalog will assist researchers and practitioners in selecting appropriate data sources for 3D city model preparation and urban environment simulation, depending on their purposes and target areas.
2. Integration of open geospatial data. We propose a tool that automates the integration of publicly available geospatial data to generate semantic 3D city models. This approach enables users to prepare 3D city models and conduct urban environment simulations for cities worldwide with minimal manual effort.
3. Open-source Python package. We release our tool as an open-source Python package, allowing users to easily adopt, modify, and combine it with other Python libraries. Through this release, we aim to streamline 3D city model preparation and encourage broader collaboration and innovation within the community.

3. Review of open geospatial data

In this section, we review open geospatial data related to building height, tree canopy height, land cover, and terrain elevation, comparing spatial coverage, resolution, platform, and file format. Sections 3.1 to 3.4 discuss each data type in detail. To select data sources to review, we set two criteria: (1) global or multinational coverage and (2) horizontal resolution finer than 10 m. We set this 10 m threshold, following previous studies that employ 10 m as the maximum mesh size for wind and microclimate simulation [101, 102, 103]. Additionally, our data review has not incorporated existing 3D city models such as Project PLATEAU for Japan[8] because this work specifically focuses on contributing to cities without such available models. This limitation is discussed in Section 5.1. Based on this review, we present a comprehensive data catalog in Section 3.5 to guide readers in selecting suitable data sources for specific target areas and research purposes.

[6] https://github.com/
[7] https://pypi.org/
[8] https://www.mlit.go.jp/plateau/open-data/

3.1. Building height

Following the aforementioned criteria for spatial coverage and resolution, we selected OpenStreetMap[9] (OSM), Overture[10], EUBUCCO v0.1[11] [104], UT-GLOBUS [22], Open Buildings 2.5D Temporal dataset (OB2.5DT) [26], and Microsoft Building Footprints (MSBF) [105] for review. Table 1 summarizes their characteristics. None of these sources provides complete, worldwide coverage, underscoring the importance of selecting a dataset that best suits the target city.

Table 1: Comparison of building height data sources. RMSE and MAE denote Root Mean Squared Error and Mean Absolute Error, respectively.

Dataset	**Spatial Coverage**	**Resolution /Accuracy**	**Platform /File format**	**Source /Data Acquisition**
OpenStreetMap	Worldwide (24% completeness in city centers [106])	- / Not provided	API / JSON (vector)	Volunteered / updated at irregular intervals
Overture	Worldwide	- / Not provided	API / JSON (vector)	OpenStreetMap, Esri Community Maps Program, Google Open Buildings, etc. / updated at irregular intervals
EUBUCCO v0.1 [104]	27 EU countries and Switzerland (378 regions and 40,829 cities)	- / Not provided	Files on the official website (`https://eubucco.com/`), Zenodo / GPKG (vector)	OpenStreetMap, government datasets / 2003-2021 (majority is after 2019)
UT-GLOBUS [22]	Worldwide (more than 1200 cities or locales)	- / 7.8 m (RMSE, height)	Files on Zenodo / GPKG (vector)	Prediction from building footprints, population, spaceborne nDSM / not provided
Microsoft Building Footprints [105]	North America, Europe, Australia	- / Not provided	List of download links with QuadKey / GeoJSON (vector)	Prediction from satellite or aerial imagery / 2018-2019 for the majority of the input imagery
Open Buildings 2.5D Temporal dataset [26]	Africa, Latin America, and South and Southeast Asia	4 m / 1.5 m (MAE, height)	Google Earth Engine, Google Cloud Storage / GeoTIFF (Raster)	Prediction from satellite imagery / 2016-2023

Figure 2 illustrates building height maps from the reviewed sources for Paris, Rio de Janeiro, and Nairobi. In OSM, some buildings lack footprints, and some footprints lack height attributes, reflecting its nature as Volunteered Geographic Information (VGI) [107]. Moreover, while OSM has higher coverage for footprints and heights in central areas of major cities (e.g., Paris and Rio de Janeiro), coverage in rural areas (e.g., Nairobi) is often poor. Overture displays coverage similar to OSM in Paris and Rio de Janeiro, but differs in footprint geometries and height values. For Nairobi, it offers substantially better footprint coverage than OSM. We attribute such differences to Overture's data acquisition strategy: it uses OSM as a baseline and augments coverage with other sources, including MSBF, Google Open Buildings, and the Esri Community Maps Program (as detailed in their documentation: `https://docs.overturemaps.org/guides/buildings`). EUBUCCO exhibits higher completeness than both OSM and Overture in Europe, often providing more detailed footprints. This is partly due to the inclusion of governmental datasets in addition to those from OSM. OB2.5DT covers most buildings and suggests reasonably good height accuracy for low- and mid-rise buildings; however, it underestimates tall buildings exceeding 100 m. In contrast, MSBF and UT-GLOBUS tend to have lower footprint accuracy than OSM, Overture, and EUBUCCO; some footprints deviate significantly from actual building outlines, and multiple buildings can appear as a single merged footprint.

[9] `https://www.openstreetmap.org`
[10] `https://overturemaps.org`
[11] `https://eubucco.com/`

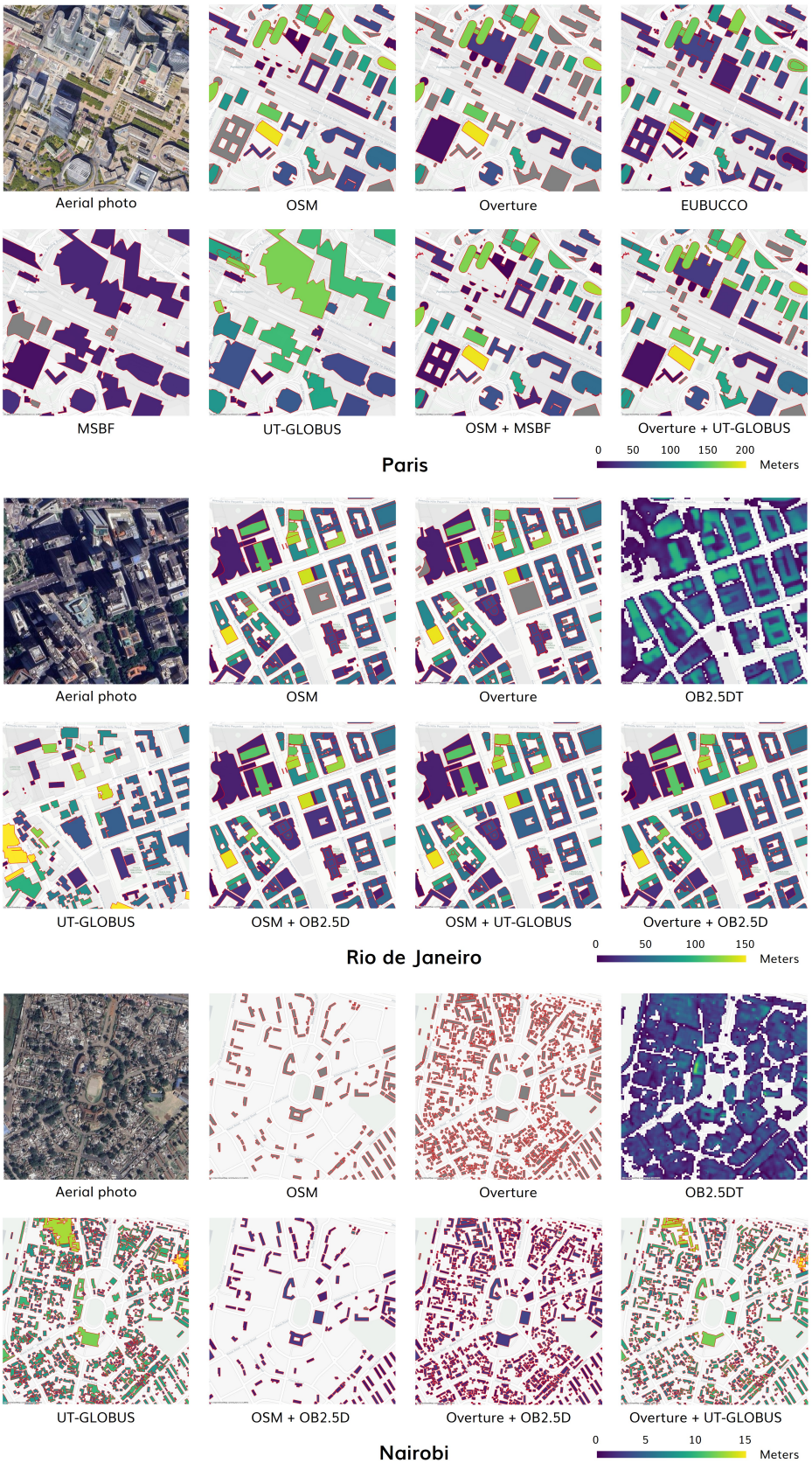

Figure 2: Examples of building height maps for Paris, Rio de Janeiro, and Nairobi. Gray indicates buildings without height data. Basemap: © OpenStreetMap contributors, © CARTO. Imagery: Google satellite tiles.

Overall, OSM, Overture, and EUBUCCO demonstrate sufficient quality for many applications, whereas MSBF, UT-GLOBUS, and OB2.5DT are less suited as sole sources for 3D city model generation. They can, however, serve as complementary data for missing building heights in EUBUCCO, OSM, and Overture. In Figure 2, the panels labeled "OSM + [dataset]" and "Overture + [dataset]" illustrate the integration of OSM or Overture footprints with either MSBF, UT-GLOBUS, or OB2.5DT. Where OSM or Overture footprints lack a height value, the missing attribute is retrieved from the intersecting footprints in a complementary data source. If a building intersects multiple footprints, the final height is determined by a weighted average based on intersection area. The resulting combined data exhibit more complete height coverage than OSM or Overture alone.

Based on this review, we decided to use EUBUCCO, OSM, and Overture as base building height data. OB2.5DT, UT-GLOBUS, and MSBF are used as complementary sources to fill in missing values.

3.2. Land cover

To select data sources for review, we set criteria requiring land cover classes suitable for general urban environment simulations, in addition to the aforementioned criteria for spatial coverage and resolution. Therefore, we excluded datasets that are restricted to specific land cover types (e.g., ice, crop, or forest) [108, 109, 110, 111].

As a result, we selected ESA World Cover 10 m 2021 V200 (ESA) [24], Esri 10m Annual Land Cover (2017-2023) (Esri) [112], Dynamic World V1 (DW) [113], OpenStreetMap[12] (OSM), OpenEarthMap Japan (OEMJ) [114], and UrbanWatch (UW) [115] for our further review. Although OEMJ and UW each cover only one nation, we included them because of their exceptionally high (1 m) resolution. Table 2 compares key metrics for these sources.

Table 2: Comparison of land cover data sources.

Dataset	**Classes**	**Spatial Coverage**	**Resolution /Accuracy**	**Platform /File format**	**Source /Data Acquisition**
ESA World Cover 10 m 2021 V200 [24]	Tree cover, Shrubland, Grassland, Cropland, Built-up, Bare/Sparse vegetation, Snow and ice, Permanent water bodies, Herbaceous wetland, Mangroves, Moss and lichen	Worldwide	10 m / 76.7%	Google Earth Engine, Zenodo / GeoTIFF (Raster)	Prediction from satellite imagery / 2021
Esri 10m Annual Land Cover (2017-2023) [112]	Water, Trees, Flooded Vegetation, Crops, Built Area, Bare Ground, Snow/Ice, Clouds, Rangeland	Worldwide	10 m / 85%	Google Earth Engine / GeoTIFF (Raster)	Prediction from satellite imagery / 2017-2023
Dynamic World V1 [113]	Water, Trees, Grass, Flooded vegetation, Crops, Shrub and scrub, Built, Bare, Snow and ice	Worldwide	10 m / 73.8%	Google Earth Engine, Zenodo / GeoTIFF (Raster)	Prediction from satellite imagery / updated daily
OpenStreetMap	Bare rock, Rock, Sand, Desert, Grass, Park, Industrial, Construction, Railway, Parking, Highway, Wood, Forest, Tree, Water, Waterway, Bay, Ocean, Farmland, Building, etc.	Worldwide	- / Not provided	API / JSON (vector)	Volunteered / updated at irregular intervals
OpenEarthMap Japan [114]	Bareland, Rangeland, Developed space, Road, Tree, Water, Agriculture land, Building	Japan	~1 m / 80%	Webmap (downloadable as tiles) / PNG (Raster)	Prediction from aerial imagery / 1974-2022 (mostly after 2018 in major cities)
UrbanWatch [115]	Building, Road, Parking Lot, Tree Canopy, Grass/Shrub, Agriculture, Water, Barren, Other	22 major cities in the US	1 m / 92%	Google Earth Engine, Google Drive / GeoTIFF (Raster)	Prediction from aerial imagery / 2014–2017

Figure 3 shows example land cover maps from the reviewed datasets for Osaka, Los Angeles, and São Paulo. To allow direct comparisons, we harmonized the class definitions across all datasets

[12] `https://www.openstreetmap.org`

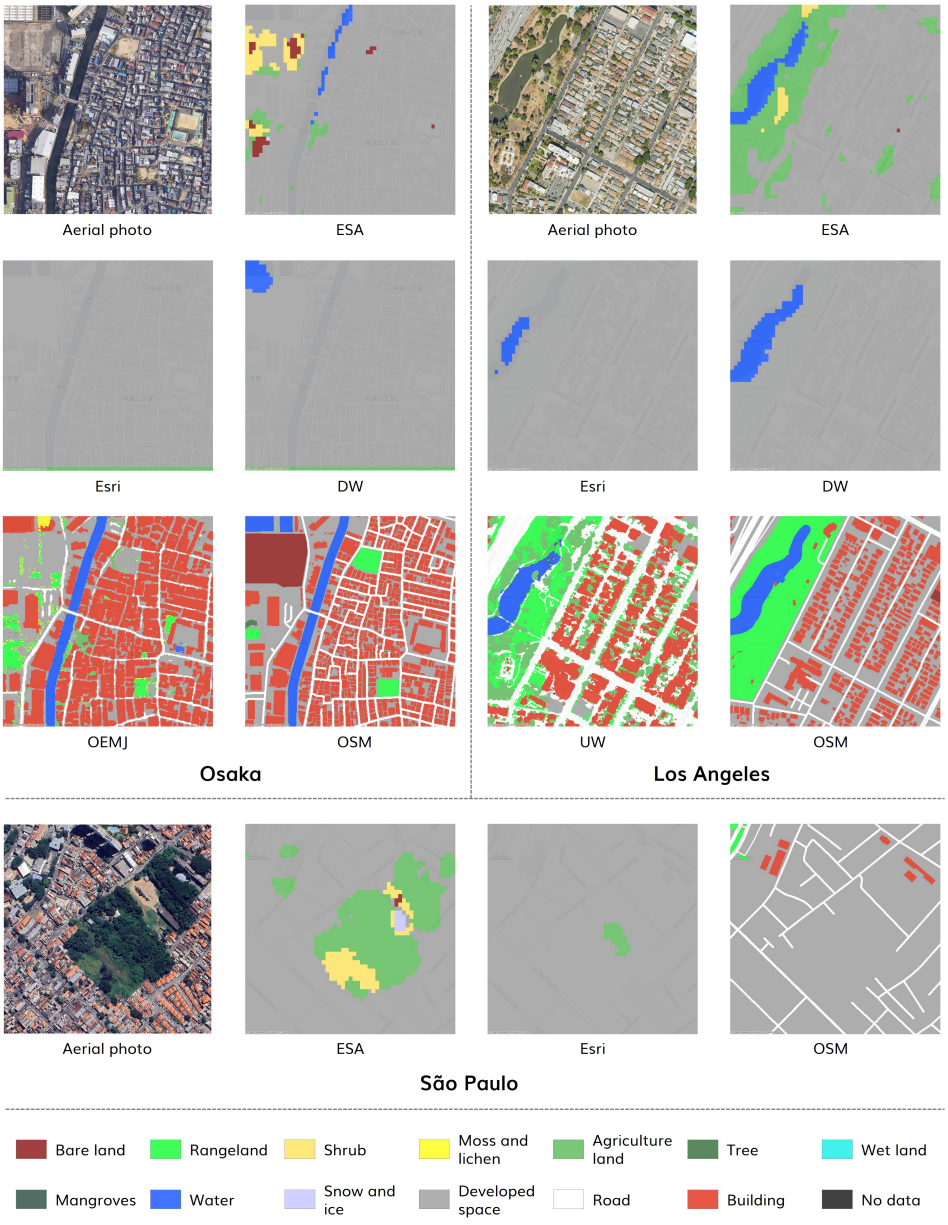

Figure 3: Examples of land cover data for Osaka and Los Angeles. Basemap: © OpenStreetMap contributors, © CARTO. Imagery: Google satellite tiles.

using the conversion rules presented in Table 3. Overall, OEMJ (for Osaka) and UW (for Los Angeles) most closely match the actual land cover when compared to aerial imagery. OSM also aligns well but tends to miss smaller patches of vegetation (particularly trees). ESA captures major water bodies and broad vegetation patterns but is less detailed than OEMJ, UW, or OSM. In OSM, some areas (e.g., São Paulo) lack detail in spatial variation, indicating lower completeness than ESA. Esri and DW indicate low completeness, classifying most pixels as "Developed space" despite these areas actually containing diverse classes. We attribute the relatively low performance of Esri and DW to their primary focus not being on urban areas, resulting in training and validation data that lacks detailed annotations for urban regions. It is important to note that, while this is not applicable to the examples in Figure 3, OSM sometimes misses the water class for oceans because some ocean areas in OSM lack water object patches.

Table 3: Class definition harmonization across different land cover data sources.

Class	**Allocated classes**					
	ESA	Esri	DW	OEMJ	UW	OSM
Bareland	Barren/sparse vegetation	Bare Ground	Bare	Bareland	Barren	quarry, brownfield, bare_rock, scree, shingle, rock, sand, desert, landfill, beach
Rangeland	Grassland	Grass	Grass	Rangeland	Grass/Shrub	grass, meadow, grassland, heath, garden, park
Shrub	Shrubland	Scrub/Shrub	Shrub and Scrub	Shrub	–	scrub, shrubland, bush, thicket
Agriculture land	Cropland	Crops	Crops	Agriculture	Agriculture	farmland, orchard, vineyard, plant_nursery, greenhouse_horticulture, flowerbed, allotments
Tree	Trees	Trees	Trees	Tree	Tree Canopy	wood, forest, tree, tree_row
Moss and lichen	Moss and lichen	–	–	–	–	moss, lichen, tundra_vegetation
Wet land	Herbaceous wetland	Flooded Vegetation	Flooded Vegetation	Wetland	–	wetland, marsh, swamp, bog, fen
Mangrove	Mangroves	–	–	Mangrove	–	mangrove, mangrove_forest, mangrove_swamp
Water	Open water	Water	Water	Water	Water, Sea	water, waterway, reservoir, basin, bay, ocean, sea, river, lake
Snow and ice	Snow and ice	Snow/Ice	Snow and Ice	Snow	–	glacier, snow, ice, snowfield, ice_shelf
Developed space	Built-up	Built Area	Built	Developed	Parking Lot	industrial, retail, commercial, residential, construction, railway, parking, islet, island
Road	–	–	–	Road	Road	highway, road, path, track, street
Building	–	–	–	Building	Building	building, house, apartment, commercial_building, industrial_building
No Data	–	No Data, Clouds	–	–	Unknown	unknown, no_data, clouds, undefined

Based on this review, we excluded Esri and DW, and included the remaining datasets as data source options in our package.

3.3. Tree canopy height

To screen datasets, we set criteria: (1) coverage of urban areas and (2) no restriction to specific tree species, in addition to the aforementioned criteria for spatial coverage and resolution. Therefore, we excluded datasets that focus on forested regions or specific tree species [116, 117]. We also considered open tree inventories, which typically include a database of individual trees (e.g., location, size, age, species) [118, 119, 120]. However, each city or country tends to maintain its own tree inventory format, and coverage rarely extends beyond one locality [121, 122, 123]. Hence, no standardized globally comprehensive tree inventory dataset was identified. Ultimately, we selected the High Resolution 1 m Global Canopy Height Maps (META) [23] and ETH Global Sentinel-2 10 m Canopy Height (2020) (ETH) [124] for further review. Table 4 provides details on these data sources.

Figure 4 compares canopy height maps from META and ETH for areas in London and Melbourne, alongside corresponding street-level and satellite images. In London, the street-level photo indicates trees over 10 m tall (judging from the height of double-decker buses), while META reports around 3 m and ETH 12 m for the same location, suggesting underestimation by META and

Table 4: Comparison of tree canopy height data sources

Dataset	**Coverage**	**Resolution /Accuracy**	**Platform /File format**	**Source /Data Acquisition**
High Resolution 1 m Global Canopy Height Maps [23]	Worldwide	1 m / 2.8 m (MAE)	Google Earth Engine / GeoTIFF (Raster)	Prediction from satellite imagery / 2009 and 2020 (80% are 2018-2020)
ETH Global Sentinel-2 10 m Canopy Height (2020) [124]	Worldwide	10 m / 6.0 m (RMSE)	Google Earth Engine / GeoTIFF (Raster)	Prediction from satellite imagery / 2020

Figure 4: Examples of canopy height data for London and Melbourne. Basemap: © OpenStreetMap contributors, © CARTO. Imagery: Google street view, Google satellite tiles.

more accurate performance by ETH. Meanwhile in Melbourne, ETH detects a canopy height of around 10 m at a location that is primarily grass in street-level and aerial imagery, whereas META shows almost no canopy. In this case, META appears more accurate, and ETH overestimates. In short, META and ETH underestimate and overestimate canopy height, respectively, in certain situations. Neither dataset consistently outperforms the other, so the choice depends on regional characteristics and research requirements. We therefore include both options in our package, allowing users to select according to their needs.

3.4. Terrain elevation

To select terrain elevation datasets, we set a resolution threshold of 1 Arc second (30.9 m at the equator) instead of 10 m for other data types. This exception was made because, for terrain elevation data with global coverage, only datasets with resolutions coarser than 1 Arc second are available. We allowed this coarser resolution because terrain elevation in urban areas rarely changes drastically at spatial scales less than 30 m. Additionally, we established a criterion requiring a bare-earth model to exclude DEMs or DSMs that retain building and vegetation heights [125, 126, 127, 128]. Consequently, we selected Forest And Buildings removed Copernicus 30m DEM (FABDEM) [25], DeltaDTM [129], USGS 3DEP 1m DEM (USDEM) [130], England 1m Composite DTM (ENGDTM) [131], Australian 5M DEM (AUSDEM) [132], and RGE Alti (FRADEM) [133] for further review. While USDEM, ENGDTM, AUSDEM, and FRADEM have only national coverage, they were incorporated because of their exceptionally fine spatial resolution, ranging from 1 to 5 m.

Table 5 summarizes the characteristics of the selected datasets. FABDEM provides the most extensive worldwide coverage, followed by DeltaDTM, which covers global coastal areas. While the other datasets are limited to country-scale coverage, they offer superior horizontal resolutions ranging from 1 to 5 m—significantly finer than those of FABDEM and DeltaDTM.

Table 5: Comparison of terrain elevation data sources

Dataset	**Coverage**	**Resolution /Accuracy**	**Platform /File format**	**Source /Data Acquisition**
FABDEM [25]	Worldwide	30 m / Built-up areas: 1.12 m, forests: 2.88 m (MAE)	Google Earth Engine / GeoTIFF (Raster)	Correction of Copernicus DEM using canopy height and building footprints data / 2011-2015 (Copernicus DEM)
DeltaDTM [129]	Worldwide (Only for coastal areas below 10m + mean sea level)	30 m / 0.45 m (MAE)	Google Earth Engine / GeoTIFF (Raster)	Copernicus DEM, spaceborne LiDAR / 2011-2015 (Copernicus DEM)
USGS 3DEP 1m DEM [130]	United States	1 m / Not provided	Google Earth Engine, government website / GeoTIFF (Raster)	Aerial LiDAR / 2004-2024 (mostly after 2015)
England 1m Composite DTM [131]	England	1 m / 0.15 m (RMSE, a vertical accuracy of LiDAR used)	Google Earth Engine, government website / GeoTIFF (Raster)	Aerial LiDAR / 2000-2022
Australian 5M DEM [132]	Australia	5 m / 0.30 m (error metric not specified)	Google Earth Engine, government website / GeoTIFF (Raster)	Aerial LiDAR / 2001-2015
RGE Alti [133]	France	1 m / 0.2 m (RMSE, coastal areas), 0.5 m (RMSE, large forest areas)	Google Earth Engine / GeoTIFF (Raster)	Aerial LiDAR / Not provided

Figure 5 illustrates example terrain elevation maps for London and New York City derived from the reviewed sources. ENGDTM and USDEM show more detailed spatial variation than the other

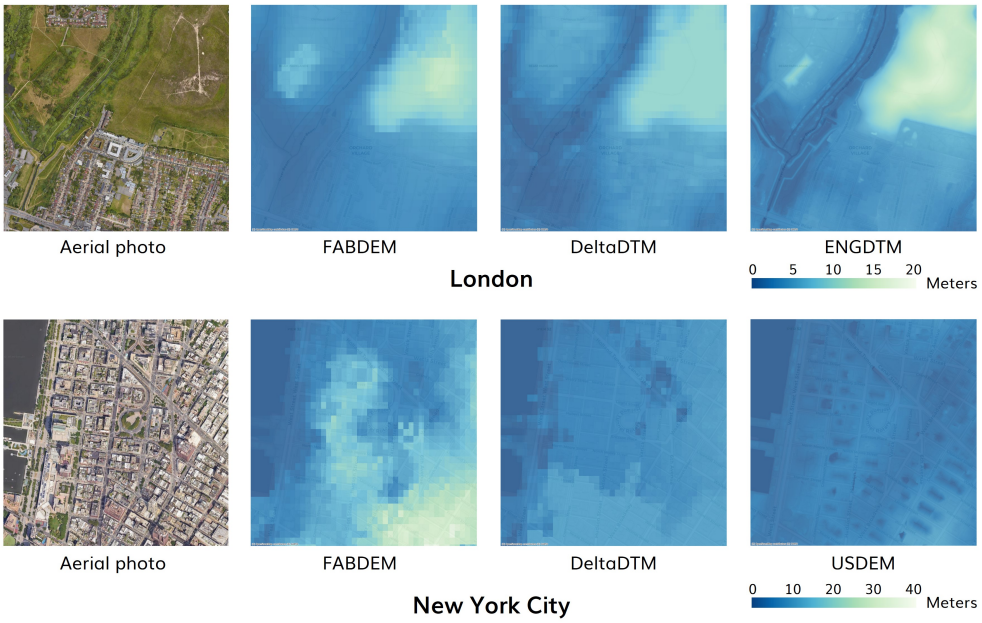

Figure 5: Examples of terrain elevation data for London and New York City. Basemap: © OpenStreetMap contributors, © CARTO. Imagery: Google satellite tiles.

datasets, consistent with their finer resolutions. The London maps display similar elevation values across all sources, whereas the New York City maps show significant discrepancies, particularly between FABDEM and USDEM. We attribute these differences to the varying methods and resulting accuracy in removing building heights in areas with dense high-rise constructions.

Based on the observed advantages and disadvantages of each dataset in terms of coverage and resolution, we decided to include all reviewed sources as options in our package.

3.5. Data catalog with guidelines for data selection

After reviewing data sources for building height, land cover, tree canopy height, and terrain elevation, we compile a comprehensive data catalog for our package (Table 6). This catalog includes guidelines to select appropriate data sources for each data type. Users can refer to this catalog to identify the most suitable data sources based on their specific target areas and research objectives.

Table 6: Catalog of data types for 3D city model generation.

Type	Data sources	Guidelines for selection
Building height	Base: EUBUCCO [104], OSM, Overture Complementary: OB2.5DT [26], UT-GLOBUS [22], MSBF [105]	(1) Use EUBUCCO for EU countries; for other regions, employ OSM or Overture as the base source. (2) If the target area is covered by any complementary dataset (MSBF for the USA, Europe, and Australia; OB2.5DT for Africa, South Asia, South-East Asia, Latin America and the Caribbean; UT-GLOBUS for 1,200 global cities), use it as the complementary source.
Land cover	UW [115], OEMJ [114], OSM, ESA [24]	(1) Use UW for U.S. cities and OEMJ for Japanese cities, where available. (2) For all other regions, rely on OSM by default. (3) If OSM coverage is insufficient, switch to ESA.
Canopy height	META [23], ETH [124]	Select either META or ETH according to the target areas and research objectives, keeping in mind that META typically underestimates canopy height while ETH tends to overestimate.
Terrain elevation	USDEM [130], ENGDTM [131], AUSDEM [132], FRADEM [133], DeltaDTM [129], FABDEM [25]	(1) For cities covered by high-resolution datasets (ENGDTM, USDEM, AUSDEM, and FRADEM), use those data sources. (2) For other regions, use FABDEM or DeltaDTM. Note that, in areas with dense high-rise buildings, these data may include significant errors.

4. The VoxCity package

In this section, we introduce 'VoxCity', an open-source Python package for open geospatial data integration, grid-based 3D city model generation, and urban environment simulation. Figure 6 illustrates the framework of VoxCity. Users start the process by specifying the target area and voxel size and selecting data sources from our catalog. The workflow consists of four main sub-processes: (1) 3D city model generation, (2) simulation, (3) file export, and (4) visualization. In (1) 3D city model generation, VoxCity downloads building height, land cover, tree canopy height, and terrain elevation data from the selected sources within the specified target area. It then voxelizes all the downloaded data and integrates them into a semantic 3D city model. In (2) simulation, the output models can be used directly to conduct urban environment simulations through VoxCity's built-in simulation functions. In (3) file export, VoxCity can export the output model in multiple file formats that are compatible with external software. In (4) visualization, VoxCity offers 3D visualization functionality for not only generated city models but also simulation results.

4.1. 3D city model generation

4.1.1. Download

VoxCity automatically downloads the required data within a target area through either file links or APIs depending on selected data sources. Users can define the target area as a rectangular region. Downloaded data are saved in users' environments and utilized in subsequent processes. Vector and raster data are saved as GeoJSON and GeoTIFF files, respectively. Users who need these intermediate files can also use VoxCity solely as a downloader for various geospatial datasets, similar to OSMnx [99], which often serves as a downloader for road networks from OSM.

4.1.2. Voxelization and integration

Downloaded data are then voxelized using voxel units through the following processes.

VoxCity first aggregates values using a two-dimensional horizontal grid defined by the voxel size (in meters). For building height, tree canopy height, and land cover, each cell's value is determined by the dominant value within that cell. For instance, focusing on land cover, when a cell includes multiple classes, the class that covers the largest area is assigned as the representative value of the cell. In this process, the land cover class harmonization shown in Table 3 is applied, enabling users to easily compare the generated 3D models across different data sources and select the desirable sources. For terrain elevation, the representative value of a cell is calculated as the average within the cell.

A voxel model is then generated for each data type by extruding the aggregated cell values. For building height, tree canopy height, and terrain elevation, two-dimensional grids are extruded corresponding to the value of each cell and its voxel size. For example, if a cell representing building height has a value of 50 m and the voxel size is 5 m, it is extruded into 10 (=50/5) voxels vertically. Tree and terrain voxels are generated using the same method. For trees, the canopy height value includes a gap between the terrain surface and the bottom of the canopy. Tree voxels occupy only the space between the top and bottom of the canopy, while void voxels fill the space below the canopy. The height of this gap is determined by multiplying the canopy height by a trunk height ratio, which can be adjusted to reflect different regions or tree species. For land cover, the topmost (surface) terrain voxel in each cell of the 2D grid is replaced with a land cover voxel.

Finally, voxel models of buildings, trees, and terrain with land cover are integrated into a single 3D city model. In this integration process, building and tree models are placed on top of the land cover voxels (the surface voxels of the terrain model).

In OSM, some buildings consist of multiple footprint polygons with detailed height information for both the top and the bottom. Such footprints represent more complex building shapes than simple extrusions based on terrain surfaces. For these buildings, our method uses both top and bottom height values to fill building voxels only between the two heights, leaving voxels between the terrain surface and the building's bottom as void (see Figure 7-Singapore as an example). Additionally, VoxCity generally does not support civil engineering structures such as bridges and elevated highways, except for some rare cases where such objects are registered with height values in OSM.

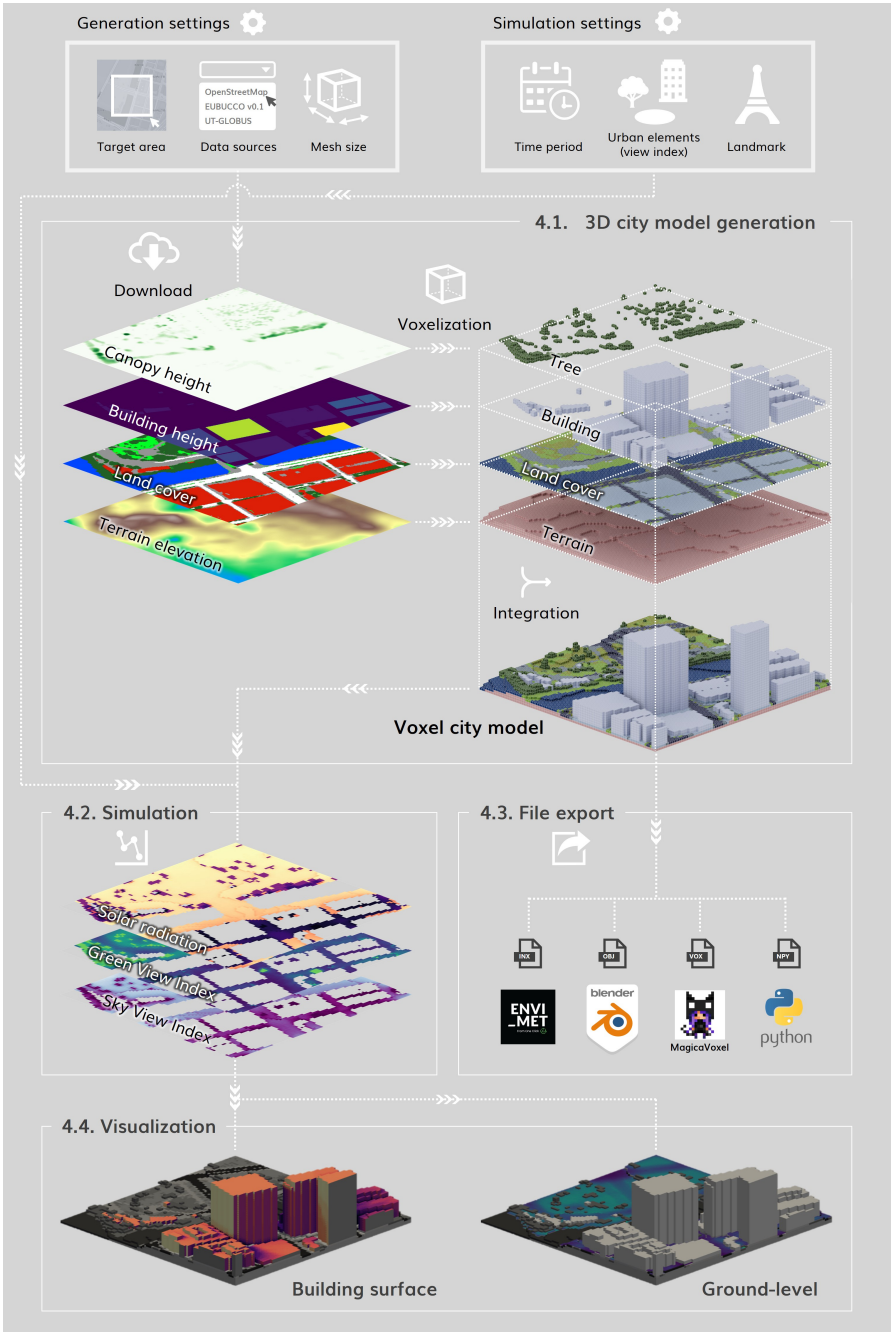

Figure 6: Workflow of data processing in 'VoxCity' – from bringing together disparate urban data sources to conducting complex multi-modal simulations – all in a single software package.

VoxCity's 3D city models are structured as three-dimensional arrays, whose dimensions correspond to the geospatial x, y, and z axes as shown in Figure B.13 in Appendix. Each cell corresponds to a voxel, and its value represents an element type such as a building, tree, or water. While some previous studies implemented octrees for voxel model structures to enhance efficiency in data processing [36, 134], VoxCity does not currently use this approach. Incorporating octrees could reduce memory usage and improve ray-tracing-based simulation performance; therefore, we plan to implement this structure in future work.

4.1.3. Example outputs

Figure 7 shows example 3D city models generated by VoxCity. These include models of Singapore, Tokyo, Paris, New York City, Rio de Janeiro, Abu Dhabi, Sydney, and Cape Town, demonstrating VoxCity's capability to generate 3D city models worldwide and in varied urban morphologies. These outputs also illustrate VoxCity's ability to represent building configurations more complex than simple extrusions of building outlines. This is particularly evident in the Singapore model, which features a rooftop park supported by three towers.

VoxCity's outputs capture the morphological characteristics of each city by combining building shapes and arrangements, land cover, tree canopies, and terrain elevations. Notable examples include the radiating block arrangements and street networks around Arc de Triomphe in Paris; dense skyscrapers surrounded by water in Lower Manhattan, New York City; tightly packed houses on a mountainside in Rio de Janeiro; and sparse high-rise buildings set amid sandy terrain in Abu Dhabi. Additionally, to further demonstrate VoxCity's capability for diverse geographies worldwide, we generated models for eight cities: Vancouver, San Francisco, Medellín, La Paz, Barcelona, Nairobi, Mumbai, and Bangkok (Figure C.14 in Appendix).

To demonstrate the efficiency of our approach, we evaluated the time requirements for manual and computational processing to generate 3D city models, as shown in Table E.8 in Appendix. Manual processing includes specifying the target area and setting data sources, while computational processing includes downloading the required data and generating the voxel city models. In our test environment—equipped with an Intel Core i9-13900 processor and an internet connection with a measured download speed of 180 Mbps—VoxCity required 90 seconds for manual and 40 seconds for computational processing for the New York City model shown in Figure 7. Computational processing times can vary substantially depending on the urban morphology and selected data sources. For instance, generation of the Singapore model shown in Figure 7, which exhibits lower building density than that of New York City, required a computational processing time of 25 seconds.

4.2. Simulation

VoxCity includes a built-in subpackage 'simulator' that calculates solar irradiance, view indices, and landmark visibility in 3D city models. Combined with the 'generator' subpackage, VoxCity provides a one-stop solution for everything from 3D city model preparations to urban environment simulations, reducing the manual effort typically required to transfer data between 3D modeling software and specialized simulation tools. The following subsections detail methodologies used for each simulation.

4.2.1. Solar radiation

A module, 'solar', provides functionality for calculating global irradiance at ground-level and on building surfaces. Solar radiation is a critical factor influencing outdoor heat stress [135], thermal comfort [136, 137], urban farming [138], photovoltaic power generation [139, 140], and building energy consumption by HVAC and lighting [141, 142]. Consequently, it has profound impacts on urban sustainability and the well-being of city dwellers—underscoring its importance in urban and architectural planning. We employ a ray-tracing based calculation method for solar irradiance introduced by Pružinec and Ďuračiová [143], Monsi and Saeki [144]. The method is summarized in Appendix D. The 'solar' module offers two calculation options: (1) instantaneous solar irradiance (Wm^{-2}) at a specific timestamp and (2) cumulative solar irradiance (Whm^{-2}) over a specific period, such as a day, a month, or a year.

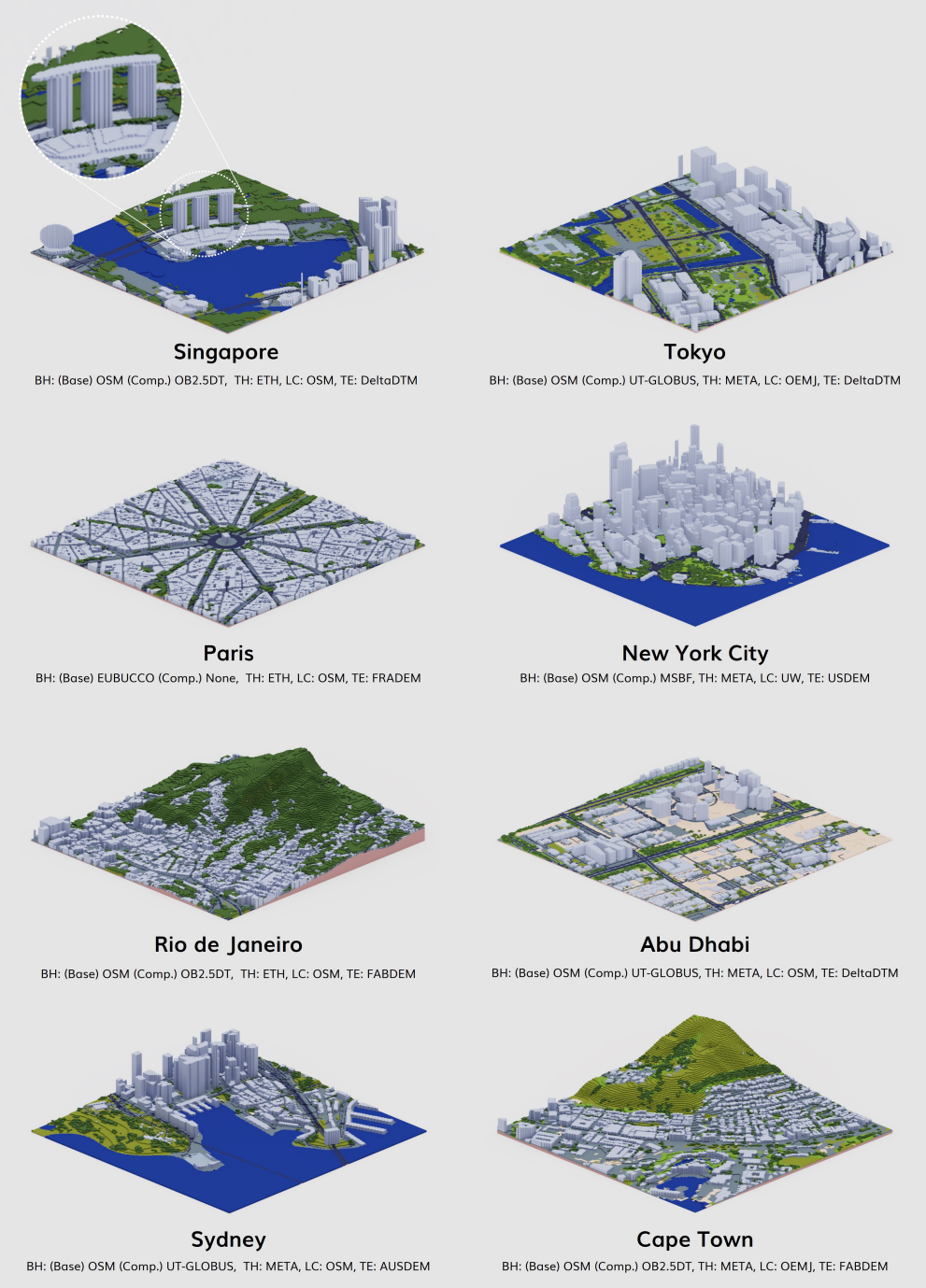

Figure 7: Examples of output 3D city models from VoxCity. 3D rendering performed in MagicaVoxel. BH, TH, LC, and TE represent building height, tree canopy height, land cover, and terrain elevation, respectively.

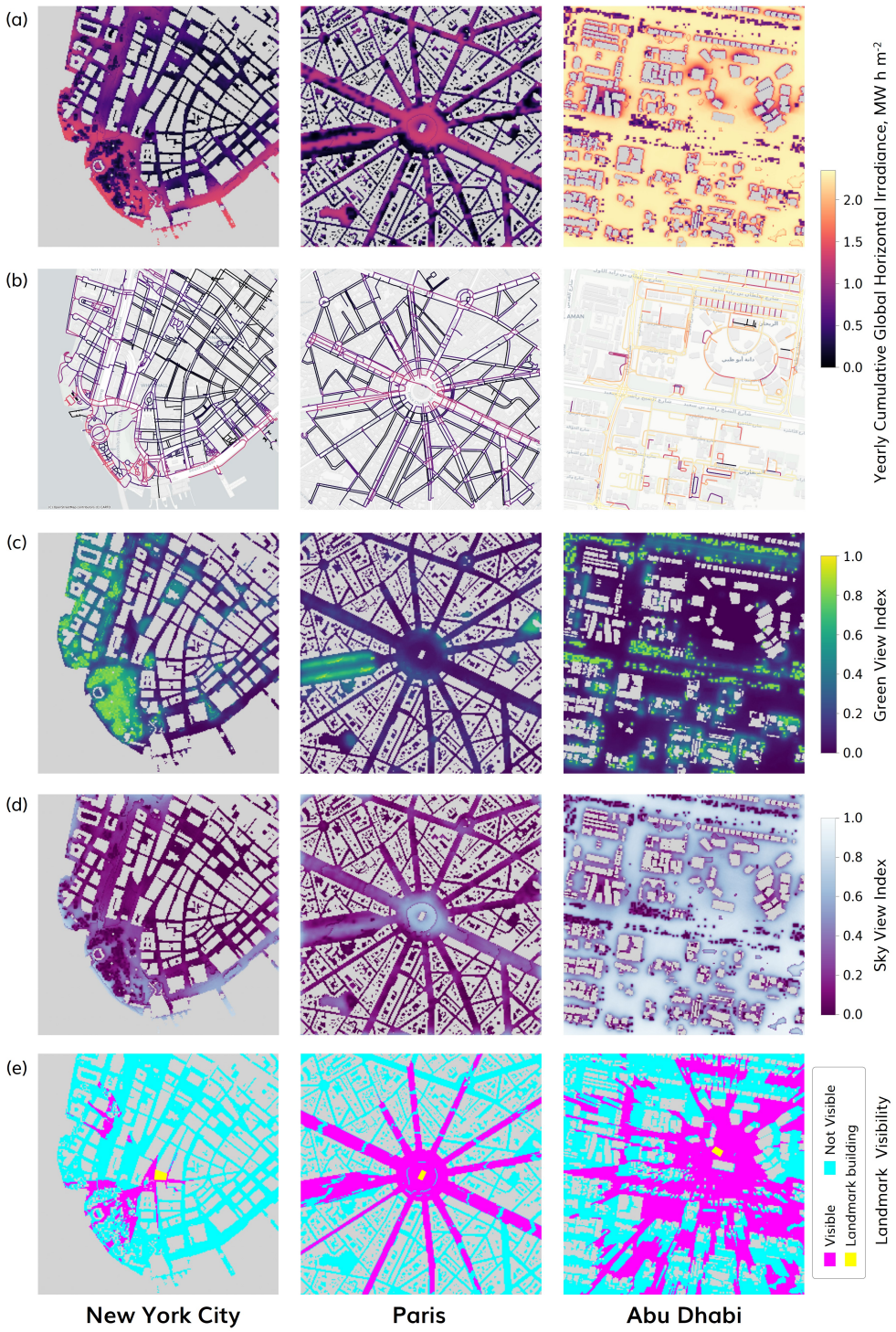

Figure 8: Example urban environment simulations conducted using 3D city models from VoxCity. (a, b) Solar irradiance. (c) Green View Index, GVI. (d) Sky View Index, SVI. (e) Landmark Visibility. Panel (b) employed walking path networks downloaded from OpenStreetMap. Basemap: © OpenStreetMap contributors, © CARTO.

Figure 8a illustrates example results of ground-level cumulative solar irradiance for three target areas: New York City, Paris, and Abu Dhabi. These simulations used the same 3D city models shown in Figure 7 and employed the nearest EPW files downloaded from Climate.OneBuilding.Org. Each target area exhibits distinct spatial variations in solar irradiance, reflecting differences in urban morphology, climate, and weather conditions. These results demonstrate the potential of VoxCity's simulation subpackage for evidence-based urban and architectural design that accounts for local conditions.

Additionally, VoxCity provides a feature to aggregate grid-based simulation results along the edges of road networks, as shown in Figure 8b. The functionality uses OSMnx to download road networks from OSM, enabling various network analyses within simulated urban environments—including not only solar irradiance but also view indices and landmark visibility, which are detailed in Section 4.2.2.

4.2.2. View index

A module, 'view', provides functionality for conducting view index analyses, where the ratio of specific object types—such as vegetation, sky, and buildings—visible from a given location is quantitatively evaluated. The module calculates the view index by applying a ray-tracing technique to 3D city models. Specifically, we implemented a line of sight evaluation method introduced by Mor et al. [145] to voxel city models. Users can specify the target object type, the vertical angle of view (i.e., the ranges in which rays are cast), and the total number of rays. The horizontal angle of view is set to 360 degrees, assuming uniform visibility in all directions.

We demonstrated the calculations of the Green View Index (GVI) and Sky View Index (SVI) using the module on 3D city models for Paris, New York City, and Abu Dhabi, as shown in Figure 8c and d. For GVI, our method casts 600 rays per location, covering 60 degrees vertically. Specifically, the vertical angles range from -30 to +30 degrees, with the horizontal direction defined as 0 degrees. Rays are cast at six-degree intervals both horizontally and vertically, resulting in $60 \times 10 = 600$ rays per location. In contrast, for SVI, areas below the horizon do not influence the results; therefore, the vertical angle of view is set from 0 to +30 degrees. This configuration produces 300 rays per location. We employed the same 3D city models shown in Figure 7. The results reflect the distinct urban morphological features of the target areas: New York City exhibits a notably low SVI due to its dense high-rise buildings, whereas Abu Dhabi shows a relatively low GVI and high SVI, aligning with its limited greenery and more sparse buildings.

The view module also provides functionality for evaluating the visibility of specified landmark buildings from ground-level locations using a ray-tracing technique. Specifically, we implemented the ground-level viewshed calculation introduced by Wróżyński et al. [146] for voxel city models. This enables users to understand from which locations within a target area the landmark buildings can be seen. Figure 8e shows example visibility maps. Landmarks play important roles in pedestrians' perception and wayfinding [147, 148], influencing visual comfort and walkability [149, 150]. The access to the view of landmarks has been proved to add property value [151]. The visibility simulations could support informed urban planning considering such effects of landmarks.

4.3. File export

VoxCity's 'exporter' subpackage can save the generated 3D city model data in several file formats to support downstream applications and data exchange. The available file formats include INX for ENVI-met [152, 153], the Wavefront OBJ for 3D modeling software, the MagicaVoxel[13] voxel model format (VOX), and the Pickle (PKL) for Python. ENVI-met is a widely used microclimate simulation software. MagicaVoxel offers GPU-accelerated 3D rendering for voxel models. PKL files enable model data transfer between different Python environments without any format conversion. When using the PKL format, the data is directly saved as a three-dimensional NumPy [154] array. For other formats, the data is first converted to each format's specific data structure. In the case of VOX, the 3D array from VoxCity is reformatted into the VOX structure, including color palette information corresponding to voxel classes. The subsequent subsections describe the export functionality for the INX and OBJ formats in more detail.

[13] `https://ephtracy.github.io/index.html`

4.3.1. INX for ENVI-met

Building height and terrain elevation from VoxCity are directly converted to the INX format, while canopy height and land cover data are translated into corresponding vegetation ID and material ID in ENVI-met before being integrated into the INX format. Table F.9 in Appendix summarizes mapping of voxel classes in VoxCity to ENVI-met material and vegetation IDs in this study. Additionally, users can specify the trunk height ratio relative to total canopy height and the leaf area density (LAD) of trees. These tree-specific settings are then exported separately as a project database (EDB) file.

Figure 9 shows microclimate simulation examples using the widely-used ENVI-met code (V5.7.1, ENVI-met Gmbh, Essen) in two characteristic sites, high-rise Al Zahiya district in Abu Dhabi and low-rise residential in Greenbelt, MD (USA). Since ENVI-met is based on the structured mesh (i.e., Cartesian coordinates), VoxCity can provide basic 3D geometries (Figures 9a and 9b) for the simulation. The calculation domains were 800 m $\times$ 800 m $\times$ 310 m for Abu Dhabi, and 500 m $\times$ 500 m $\times$ 50 m for Greenbelt. They comprised inner areas with buildings and trees with horizontally homogeneous grid spacing (4 m for Abu Dhabi and 2 m for Greenbelt here), which is off-the-shelf from VoxCity. Because perimeter margins are necessary for ENVI-met simulation to avoid unphysical results (as detailed in their documentation: `https://envi-met.com/tutorials-plugins-faqs-helpful-info/`), VoxCity provides a function to remove perimeter buildings and trees. For vertical grid spacing, VoxCity provides options that use the same size for the horizontal grid or set an arbitrary number of layers. Here, we set 19 layers for the Greenbelt case and 50 for the Abu Dhabi case. One should note that before running the simulation, ENVI-met automatically resizes the meshes within the five layers near the ground to a finer resolution. We also note that ENVI-met V5.7.1 often predicts unphysical results for complex terrains (as detailed on their website: `http://www.envi-hq.com/`), so we strongly recommend VoxCity users not to obtain DEM when conducting ENVI-met simulation.

VoxCity automatically sets default values of the thermal properties of buildings, ground, and trees by providing the INX file. Although overwriting the INX file, e.g., setting detailed building surface materials, can give more accurate predictions, we show the results with the default values here to verify their adequacy. For meteorological forcings, we used the 2004–2018 typical meteorological year data of the EnergyPlus Weather file (`https://www.ladybug.tools/epwmap/`) and selected the nearest weather stations for each site.

Figures 9c–9f show thermal environments at 1.5 m height on typical summer afternoons (2:00 p.m.), namely the horizontal wind vectors and the universal thermal climate index (UTCI) (derived from the air temperature, humidity, radiation, and wind speed) predicted by ENVI-met. In the Abu Dhabi case, the inlet wind was the northwesterly sea breeze from the Persian Gulf. The speed was relatively high above the roads and the open areas and reached 5 m/s at the maximum (Figure 9c), probably because the city block pattern is along the direction of the inlet wind. However, the inlet air temperature was 44°C, hotter than the human body, and therefore, as seen around point ① in Figure 9e for example, the increase in wind speed rather increased UTCI by convective heat transfer (see Fig. 7 of Bröde et al. [155]). Shading effects of buildings and trees on UTCI are evident, and the difference between sunlit and shaded areas reached > 20 °C (Figure 9e). Weak and complex diverged flows with lower air temperature and UTCI values are found in the leeward of the buildings (e.g., around building ② in Figures 9c and 9e and the southeast city block), indicating cooler above-roof air moved to the ground level by the downdrafts. In the Greenbelt case, the wind speed was generally lower than the inlet value (1.5 m/s) due to the momentum sink by trees (Figure 9d). The UTCI distribution seems to correspond simply to the shading pattern, and the contrast between roads and under-tree areas is evident (Figure 9f). We verified the validity of various parametric scenarios in Abu Dhabi, Greenbelt, and a few other sites. The calculations were successfully completed in all cases, while physically unrealistic results were obtained when, as mentioned above, OSM's LULC data included water surfaces or when using DEM data. Note that the validation results and limitations of the recent ENVI-met code (version 4 or above) are explained in the literature [156, 157, 158].

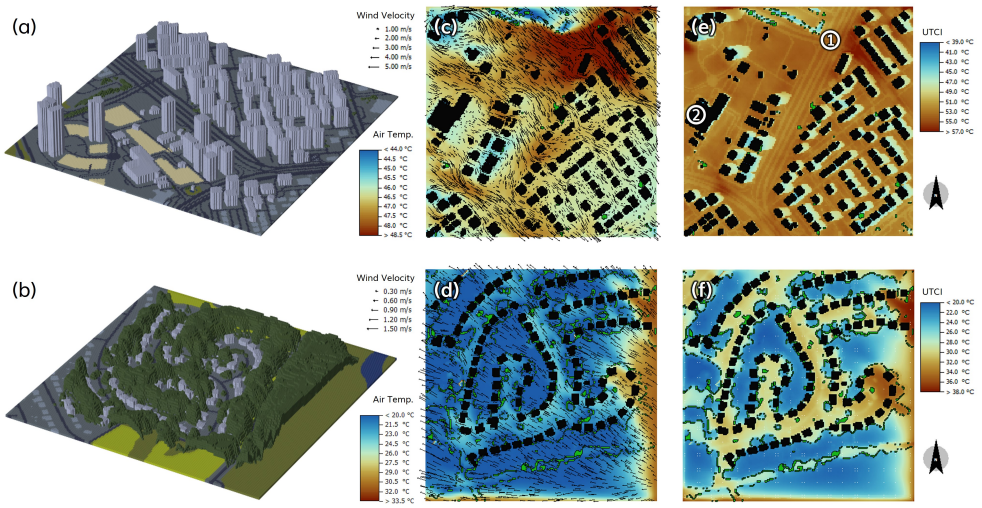

Figure 9: Examples of ENVI-met microclimate simulation in Abu Dhabi and Greenbelt. (a, b) 3D models and land-use land-cover maps obtained from VoxCity. (c, d) Horizontal wind vectors and air temperature, and (e, f) universal thermal climate index (UTCI) distributions at the 1.5-m height on typical summer afternoons.

4.3.2. OBJ for 3D modeling and rendering

The 3D array from VoxCity is converted into surface polygons of the voxel model and then formatted according to the OBJ structure. Colors corresponding to voxel classes are assigned to polygons, and the color palettes are saved as Material Template Library (MTL) files. This allows 3D modeling software to automatically apply the assigned surface colors when loading OBJ files and helps preserve semantic information that is not native to OBJ [159]. Simulation results from VoxCity's internal functions can also be exported as OBJ and MTL files.

Figure 10 shows examples of OBJ outputs rendered in Rhino 7, illustrating VoxCity's capabilities to produce diverse visualization styles for different purposes. The renderings for Singapore and New York City aim to provide photo-realistic visualization of large-scale urban morphologies. Those for Tokyo and Amsterdam employ vibrant colors for specific urban objects, vegetation, and water, highlighting distinct urban morphological features. The example of Abu Dhabi demonstrates how urban environment simulation results can be integrated with 3D city models by exporting simulation data as OBJ files. This makes it easier for viewers to understand the relationship between simulated environments and the underlying urban morphology. Although VoxCity primarily focuses on urban areas, it can also be used to visualize natural environments. In the Matterhorn example, VoxCity accurately captures the mountain's sharp peak and ice-covered terrain.

4.4. Visualization

VoxCity provides a built-in function for 3D visualization. Figure 11 shows example outputs produced by this functionality. Users can visualize generated 3D city models as well as simulation results. For instance, Figure 11a, b, c, and d indicate the yearly cumulative global irradiance on building surfaces, the ground-level sky view index, the ground-level green view index, and the ground-level landmark visibility, respectively. Users can specify projection types from two options: 'orthographic' and 'perspective', adjust the zoom factor, and change the camera position and angle.

5. Limitations and future directions

5.1. Support and integration of existing semantic 3D city models

Considering the aspiring role of VoxCity in 3D GIS, an integration of advanced 3D data models (e.g., CityGML and CityJSON) could facilitate its broader interdisciplinary adoption. In this section, we will discuss such integration in two aspects — (1) incorporating semantic 3D models as input data sources; and (2) extending export outputs to standardized 3D data formats.

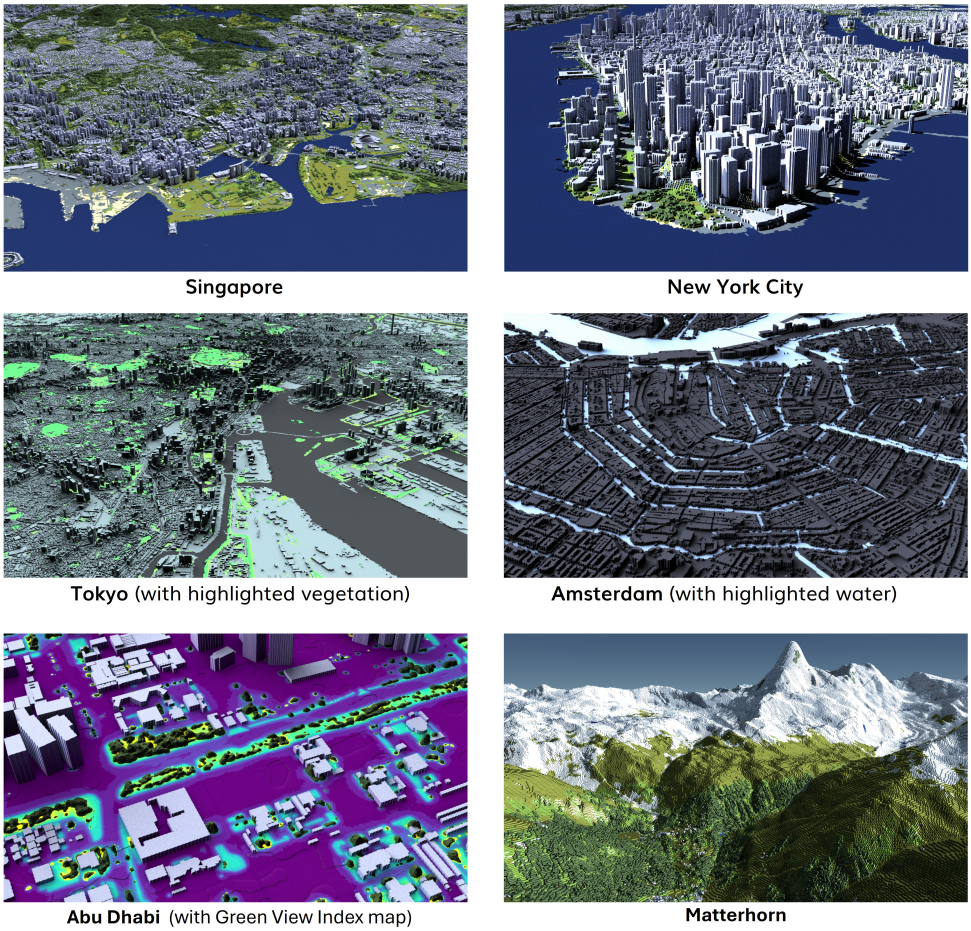

Figure 10: Examples of 3D renderings created in Rhino using output 3D city models from VoxCity.

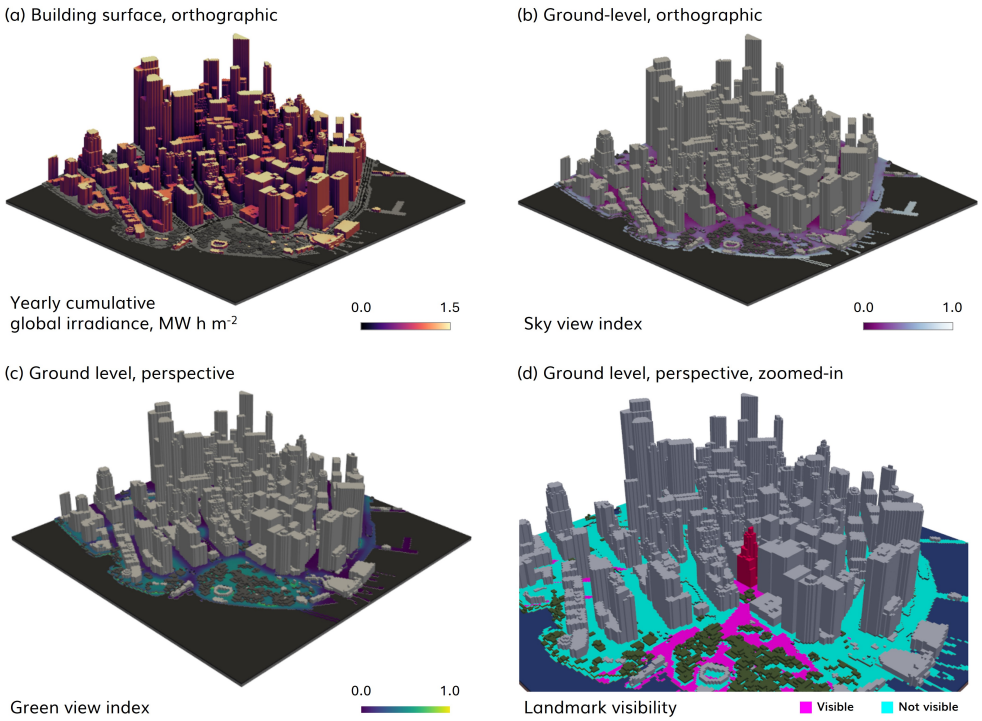

Figure 11: Example outputs for New York City produced by VoxCity's built-in 3D visualization function.

First, integrating 3D models has the potential to enrich geospatial information embedded within VoxCity, contributing to more comprehensive and tailored research. VoxCity currently generates 3D city models from a series of openly available 2D and 2.5D datasets, which can result in a lack of semantic and geometric details especially for research at block or building scale. Integration of publicly available 3D city models as supplementary input may be beneficial for such cases. For example, 3D datasets, such as 3DBAG in the Netherlands [160, 161, 87] offer higher levels of detail achieved through advanced acquisition techniques (e.g., high-resolution airborne laser scanning) and state-of-the-art reconstruction algorithms. Such 3D datasets can address current limitations in semantics and geometry, particularly in the representation of building forms (e.g., roof-related semantics) and vegetation (e.g., classification) [162]. Nevertheless, the integration of detailed semantic 3D models introduces certain trade-offs in the future development of VoxCity. Large and complex 3D datasets often entail substantial computational demands, which may hinder overall efficiency. Future research needs to evaluate the balance between the benefits of enhanced semantic detail and the associated technical costs when scaling to an extensive city scale.

Second, in the current implementation, VoxCity provides four export formats (i.e., PKL, VOX, INX, and OBJ) to interface with downstream applications. Fostering data standardization and interoperability, in the future, we plan to implement additional export options (e.g., CityGML or CityJSON). For example, exporting 3D city models in standardized formats is of value for use cases that involve data exchange and sharing with practitioners or systems, which require compliance with established schemas. By offering CityGML or CityJSON as export options, VoxCity can enhance compatibility and ensure broader usability across various domains. Further, VoxCity incorporates semantic information during the generation process; therefore, preserving these attributes through standardized formats is important. Formats such as CityJSON are ideal for this purpose, providing a compact, structured, and easy-to-use approach to storing and managing semantic data [160]. Therefore, such properties can be retained and effectively communicated for downstream practices. For example, a recent study by Lei et al. [163] extended the CityJSON schema to accommodate human perception of architectural appearance in 3D buildings, enabling potential use cases. In this work, VoxCity features its novelty in automatic generation and tangible usability. Enabling standardized export can strengthen the role of VoxCity as a versatile tool,

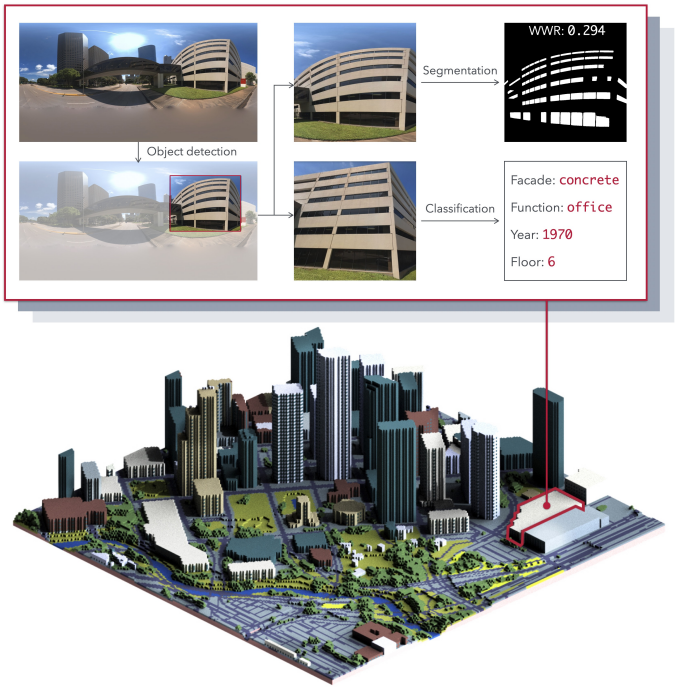

Figure 12: 3D city model of a target area in Houston, United States, from a trial incorporating building surface materials and window ratio information extracted from street view imagery. Image source: Mapillary. 3D rendering performed in Rhino.

supporting the consistent and interoperable development of 3D city models. However, challenges should be considered, such as the complexity of translating a voxel-based representation into a hierarchical structure, as well as computational and storage costs compared to current formats (e.g., PKL or OBJ).

5.2. Integration of building surface material information

Integrating building surface attributes, such as surface materials and window-to-wall ratio (WWR), into VoxCity is another promising direction for the next iteration of the package. VoxCity currently does not support the integration of building surface attributes, primarily due to limitations in data sources. To the best of our knowledge, no global open datasets currently provide surface attributes for individual buildings. While some buildings in OSM include material information, the proportion is relatively small [107]. However, building materials and WWR can significantly influence the surrounding microclimate and building energy consumption in various ways, including heat transfer, air leakage or ventilation, and offsetting daylighting demand [164, 165, 166]. This highlights the importance of incorporating material and WWR information in 3D city model generation for detailed urban environment simulations. A potential approach to address this gap is to use computer vision techniques on street view imagery to infer facade features.

In light of this, we conducted a trial to incorporate (1) building surface materials and (2) WWR information into VoxCity's 3D city model generation. Figure 12 provides an overview of the process. First, street view images were obtained from Mapillary for a target area in Houston, United States. OpenFACADES pipeline [167] was then employed to geolocate and detect buildings within the street view images, assigning them to their corresponding building footprints. Building on previous facade classification studies [168, 169, 170], we applied fine-tuned models to categorize the building materials depicted in these images [171, 172], with each footprint linked to multiple images. For WWR, window pixels were identified using the Grounded Segment Anything [173], and the percentage of window pixels within the building walls was calculated. Based on the inferred materials and WWR, we assigned categorical values to building voxels (e.g., 10 for glass, 11 for concrete, 12 for brick, and 13 for wood).

3D city models with detailed building material attributes can improve the accuracy of these simulations and expand their range of potential applications. Consequently, we plan to develop an additional subpackage that provides this functionality, after refining the methods and conducting a thorough validation.

5.3. Data availability and functionality constraints

In Section 4, we have demonstrated VoxCity's capability to generate 3D models of a variety of cities worldwide. However, we acknowledge that data availability remains a critical challenge and VoxCity does not incorporate all available data sources. Consequently, users may find it challenging to produce accurate models for regions beyond its current scope. Notwithstanding, comprehensive tools such as VoxCity play a crucial role in highlighting where data gaps remain, thereby supporting the development of targeted use cases. We are further addressing this challenge by continuously updating VoxCity and expanding the range of datasets it supports. Meanwhile, to broaden the utilization of building data, efforts to combine individual local datasets into comprehensive global collections—such as EUBUCCO [104]—should be further encouraged. Additionally, we have provided only qualitative comparisons of data sources in Section 3. To help users select the best data source options for their target areas, future work will conduct comparative experiments that provide quantitative comparisons of data sources in coverage and completeness.

Our method currently considers only tree canopy height and does not account for variations in shape and density, which can differ by species, season, and health condition. For an accurate assessment of urban environments, it is crucial to include these factors. However, such detailed information is often unavailable in most cities, although some have created tree inventories containing data on individual trees. We plan to add functionality to parse such inventories and incorporate them into model generation. As mentioned in Section 3.3, no globally comprehensive tree inventory datasets or standardized data formats currently exist. Both the integration of local inventories into a global repository and the development of standardized data structures must be pursued in parallel.

VoxCity currently does not support the ability to edit data source files. For example, users cannot edit the arrangement of buildings, trees, and land cover from the original datasets. Therefore, users cannot conduct simulations to compare different design scenarios. To further enhance usability in urban studies and urban and architectural planning practices, future work will address this limitation by developing, for instance, a user interface to interactively edit data source files and voxel city models. Additionally, the current version does not support interactive visualization, multi-dimensional data overlays, or integration with GIS platforms. These limitations represent important areas for future development of VoxCity.

6. Conclusions

Urban environment simulations using 3D city models are powerful instruments for informed urban planning and policymaking, particularly for assessing environmental benefits and risks that affect the health and well-being of city dwellers. However, the intensive manual effort required to prepare 3D city models, complicated application-specific data requirements, and fragmented data availability often hinder their broader utilization. To address this, we developed 'VoxCity', a one-stop Python package for open geospatial data integration, 3D city model generation, and urban environment simulation. Focusing on four key data types— building height, tree canopy height, land cover, and terrain elevation—we reviewed existing open datasets and compiled them into a catalog. VoxCity automatically downloads these datasets, voxelizes buildings, trees, land cover, and terrain, and creates an integrated voxel-based city model ready for a variety of environmental simulations. Additionally, VoxCity enables users to perform urban environment simulations through its built-in simulation subpackage and to export the generated 3D models in various file formats compatible with external software. The key contributions of this holistic and integrated work are as follows.

1. This paper presents a review of globally available geospatial data relevant to 3D city models—including building height, tree canopy height, land cover, and terrain elevation.

This review not only helps VoxCity users select appropriate datasets but also provides readers with an overview of such datasets.

2. VoxCity provides a streamlined and automatic method to prepare 3D city models. This is particularly advantageous in cities without openly available 3D city models. Additionally, VoxCity's capability to generate ready-to-use models for urban environment simulations benefits even those cities with existing 3D city models.
3. VoxCity can integrate four geospatial data types — building height, tree canopy height, land cover, and terrain elevation — to generate semantic 3D city models. Users can conduct simulations that account for buildings, vegetation, water bodies, and terrain geometry, all of which significantly affect urban environments.
4. VoxCity's built-in simulation and visualization functions provide a comprehensive, end-to-end solution—from 3D city model generation to running urban environment simulations including solar irradiance and visibility analyses and visualizing the simulation results—thereby significantly reducing the time and effort required for such tasks.
5. By leveraging data from OSM, which is continuously updated by volunteers, VoxCity ensures its 3D city models remain relatively current. Many open 3D city models are not continuously updated and can quickly become obsolete; however, VoxCity mitigates this limitation by providing a more up-to-date representation of the urban form.
6. VoxCity can also serve as a comprehensive data downloader, sourcing information from various providers for users who require only intermediate data.

Declaration of Competing Interest

The authors declare that they have no known competing financial interests or personal relationships that could have appeared to influence the work reported in this paper.

Declaration of Generative AI and AI-assisted technologies in the writing process

During the preparation of this work the authors used ChatGPT in order to proofread the text. After using this tool, the authors reviewed and edited the content as needed and take full responsibility for the content of the publication.

Acknowledgements

We express our gratitude to the members of the NUS Urban Analytics Lab for the valuable discussions. This research has been supported by Takenaka Corporation. This research is part of the projects (i) Large-scale 3D Geospatial Data for Urban Analytics, which is supported by the National University of Singapore under the Start Up Grant; (ii) Multi-scale Digital Twins for the Urban Environment: From Heartbeats to Cities, which is supported by the Singapore Ministry of Education Academic Research Fund Tier 1; (iii) NUS Resilience and Growth Postdoctoral Fellowship – Smart Cities and Urban Analytics, which is funded by the National Research Foundation (NRF), Singapore; (iv) Development of a Multiscale Urban Microclimate Model for NUS Campus Thermal Environment (funded by NUS). We would like to thank the Singapore International Graduate Award (SINGA) scholarship provided by the Agency for Science, Technology, and Research (A*STAR), and NUS Research Scholarship and the President's Graduate Fellowship (PGF) provided by NUS.

Data availability

The source code of VoxCity is openly available at a GitHub repository (https://github.com/kunifujiwara/VoxCity).

Appendix A. Environmental simulations and urban elements

Table A.7: Assessment categories for environmental simulation and their corresponding urban elements

Assessment categories	References	Urban elements
Thermal comfort / heat stress	Chen et al. [41], Yuan et al. [2], Lindberg et al. [1], Kong et al. [42], Li and Wang [43], Galal et al. [54], Zhang et al. [55], Hong and Lin [56], Wu et al. [57], Morakinyo and Lam [58], Li et al. [59], Wang et al. [60], Robitu et al. [66], Du et al. [67], Imam Syafii et al. [68]	Buildings, trees, land cover, terrain elevation
Sunlight exposure / photovoltaic potential	Grant et al. [53], Fath et al. [174]	Buildings, trees
Wind comfort / wind energy potential / wind pressure	Blocken et al. [49], Mou et al. [51], Hong and Lin [56]	Buildings, trees
Building energy performance	Forouzandeh [44], Gros et al. [6], Bouyer et al. [7]	Buildings, land cover (low vegetation, etc.)
Air quality	Kwak et al. [48]	Buildings, terrain elevation, air pollutant emissions
Visual comfort / green view index / sky view factor	Oh [5], Yi and Kim [72], Yu et al. [71], Labib et al. [74], Fujiwara et al. [73]	Buildings, trees, land cover, terrain elevation

Appendix B. Data structure of voxel city models

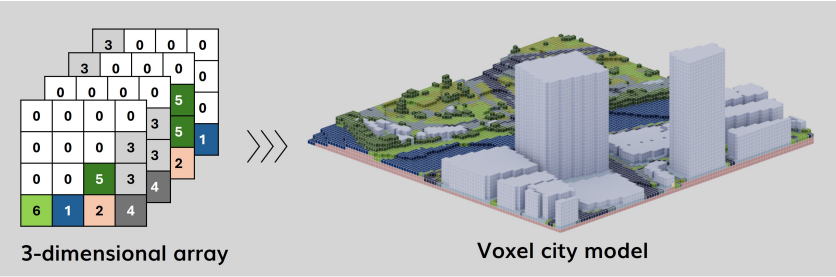

Figure B.13: 3-dimensional array representing semantic voxel city models.

Appendix C. 3D models for diverse geographies worldwide

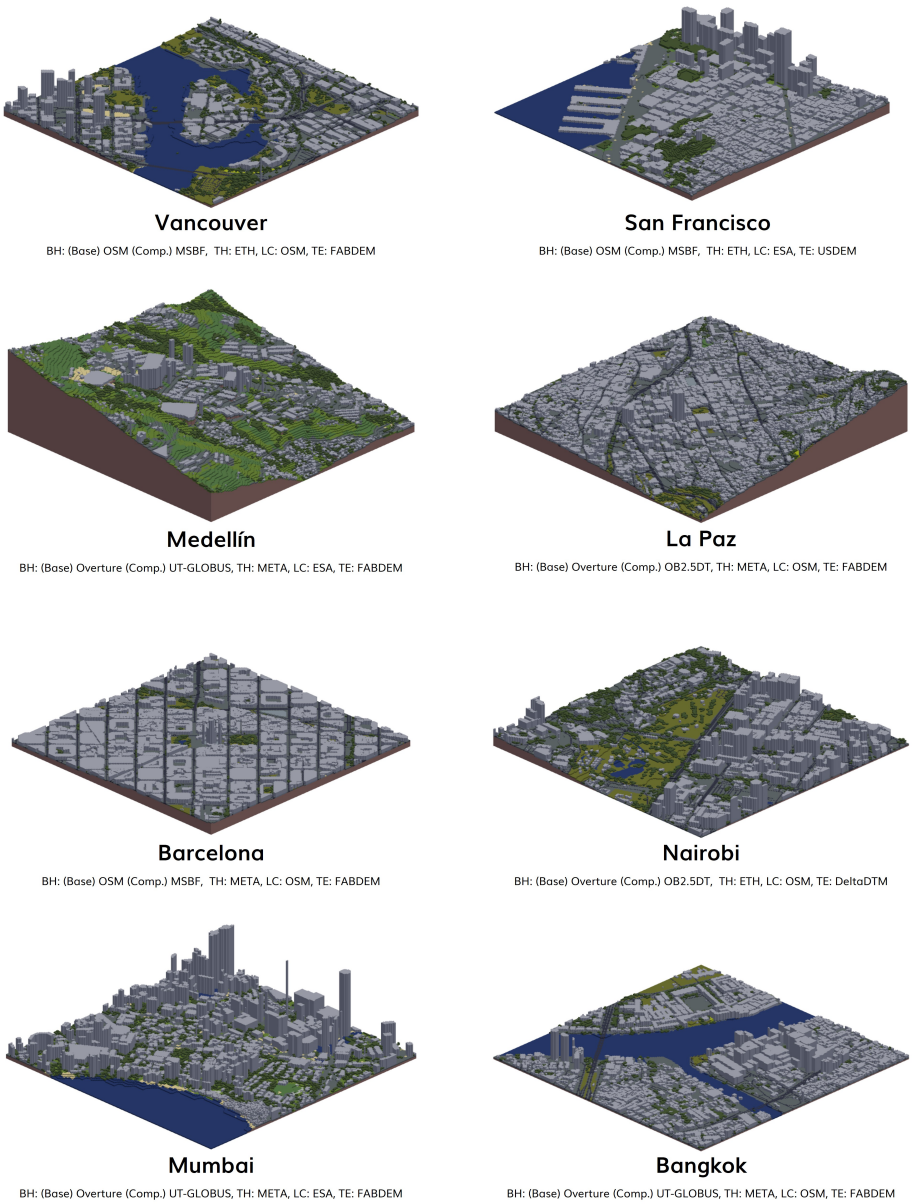

Figure C.14: Additional examples of output 3D city models from VoxCity. The 3D rendering was performed in VoxCity's visualization module. BH, TH, LC, and TE represent building height, tree canopy height, land cover, and terrain elevation, respectively.

Appendix D. Calculation of solar irradiance

We implemented a calculation combining the methods by Pružinec and Ďuračiová [143] and Monsi and Saeki [144]. Pružinec and Ďuračiová [143] introduced a ray-tracing and voxel-based method, while Monsi and Saeki [144] introduced a method to calculate transmittance of trees from leaf area density (LAD). For instantaneous values, the module first calculates solar azimuth and elevation angles using the location (longitude and latitude) of the target area and the target timestamp, employing a Python package 'astral'[14]. Direct and diffuse irradiance are then calculated using a ray-tracing technique, incorporating the computed sun position as well as direct normal and diffuse horizontal irradiance that is not affected by shading. In the ray-tracing process, a transmittance determined by the Beer-Lambert law (Equation D.1) is incorporated when rays pass through tree voxels:

$$\tau = e^{-K \cdot LAD \cdot l} \quad \text{(Monsi and Saeki [144])} \tag{D.1}$$

where τ is the transmittance of solar radiation through tree canopies, e is the base of the natural logarithm, K is the extinction coefficient, LAD represents the leaf area density ($m^2\ m^{-3}$), and l is the path length through tree voxels (m). In this paper, we employed $K = 0.5$, and $LAD = 1.0\ m^2\ m^{-3}$.

For cumulative values, the module calculates instantaneous irradiance at each timestamp from the start to the end of a specified period and then sums the results. To incorporate locally relevant climate conditions (including direct normal and diffuse horizontal irradiance), the module can use EnergyPlus Weather (EPW) files. Users may supply their own EPW files; otherwise, the module can automatically download the nearest EPW file from Climate.OneBuilding.Org [15].

Appendix E. Time requirements for 3D city model generation and simulations

Table E.8: Time requirements for 3D city model generation and simulations using VoxCity for an area in New York City. The workflow includes both manual user inputs (specifying parameters, target areas, etc.) and automated computational processes (data downloading, ray-tracing calculations, etc.). The target area, data sources, and simulation settings are the same as those in Figures 7 and 8. Processing was performed on our system with an Intel Core i9-13900 processor and an internet connection with a measured download speed of 180 Mbps.

Process	Type	Breakdown	Time required
Model generation	Manual	Specifying target area, setting data sources and parameters	90 sec
	Computational	Downloading data sources, generating a voxel city model	40 sec
Solar irradiance simulation	Manual	Setting target time range	30 sec
	Computational	Downloading the nearest weather file, ray-tracing calculation (for 8760 time steps)	50 sec
Green view index calculation	Manual	-	0 sec
	Computational	Ray-tracing calculation	1 sec
Landmark visibility analysis	Manual	Specifying landmark buildings	30 sec
	Computational	Ray-tracing calculation	1 sec

[14] https://github.com/sffjunkie/astral

[15] https://climate.onebuilding.org/

Appendix F. ENVI-met Material Mapping and Parameters

Table F.9: Mapping of voxel classes in VoxCity to ENVI-met material and vegetation IDs with their basic properties. The model uses a layered structure where vegetation and building objects are placed on top of ground/soil profiles (e.g., rangeland = grass on sandy loam; wet land = grass on water; building = wall on sandy loam).

Voxel classes in VoxCity	**Material type**	**ENVI-met material/ vegetation ID**	**Basic properties**
Bareland, Rangeland, Shrub, Moss and lichen, Agriculture land, Tree, Snow and ice, Building, No Data	Ground/soil	000000 (default sandy loam)	Albedo: 0.20, Emissivity: 0.98, Roughness: 0.015 m, Sandy loam soil profile (19 layers)
Wet land, Mangroves, Water	Ground/soil	0200WW (deep water)	Albedo: 0.00, Emissivity: 0.96, Roughness: 0.01 m, Water mixing coeff: 0.001, Turbidity: 2.1
Road	Ground/soil	0200ST (asphalt road)	Albedo: 0.12, Emissivity: 0.90, Roughness: 0.01 m, 9 layers asphalt over 10 layers sandy loam
Rangeland, Moss and lichen, Agriculture land, Wet land	Vegetation	0200XX (grass 25 cm aver. dense)	Height: 0.25 m, Albedo: 0.20, Emissivity: 0.97, Transmittance: 0.30, rs_min: 200 s/m, LAD: uniform 0.30 m^2/m^3, Root depth: 0.20 m
Shrub	Vegetation	0200H1 (hedge dense, 1 m)	Height: 1.00 m, Albedo: 0.20, Emissivity: 0.97, Transmittance: 0.30, rs_min: 400 s/m, LAD: uniform 1.00 m^2/m^3, Root depth: 1.00 m
Tree	Vegetation	- (user-defined 3D plants by canopy height)	Albedo: 0.18, Transmittance: 0.30, rs_min: 0.0 s/m, LAD: 1.0 m^{-1}, Wood density: 690 kg/m^3
Building	Building wall	000000 (default wall – moderate insulation)	3-layer (plaster/insulation/concrete), Total thickness: 0.31 m, Roughness: 0.02 m, Can be greened

References

[1] F. Lindberg, B. Holmer, S. Thorsson, SOLWEIG 1.0–modelling spatial variations of 3D radiant fluxes and mean radiant temperature in complex urban settings, Int. J. Biometeorol. 52 (2008) 697–713.

[2] J. Yuan, S. Masuko, Y. Shimazaki, T. Yamanaka, T. Kobayashi, Evaluation of outdoor thermal comfort under different building external-wall-surface with different reflective directional properties using CFD analysis and model experiment, Build. Environ. 207 (2022) 108478.

[3] I. Pađen, C. García-Sánchez, H. Ledoux, Towards automatic reconstruction of 3D city models tailored for urban flow simulations, Front. Built Environ. 8 (2022) 899332.

[4] P. R. W. Urech, M. O. Mughal, C. Bartesaghi-Koc, A simulation-based design framework to iteratively analyze and shape urban landscapes using point cloud modeling, Comput. Environ. Urban Syst. 91 (2022) 101731.

[5] K. Oh, A perceptual evaluation of computer-based landscape simulations, Landsc. Urban Plan. 28 (1994) 201–216.

[6] A. Gros, E. Bozonnet, C. Inard, M. Musy, Simulation tools to assess microclimate and building energy – a case study on the design of a new district, Energy Build. 114 (2016) 112–122.

[7] J. Bouyer, C. Inard, M. Musy, Microclimatic coupling as a solution to improve building energy simulation in an urban context, Energy Build. 43 (2011) 1549–1559.

[8] A. Katal, M. Mortezazadeh, L. l. Wang, H. Yu, Urban building energy and microclimate modeling – from 3D city generation to dynamic simulations, Energy (Oxf.) 251 (2022) 123817.

[9] J. Stoter, H. de Kluijver, V. Kurakula, 3D noise mapping in urban areas, Geogr. Inf. Syst. 22 (2008) 907–924.

[10] W.-J. Zhao, E.-X. Liu, H. J. Poh, B. Wang, S.-P. Gao, C. E. Png, K. W. Li, S. H. Chong, 3D traffic noise mapping using unstructured surface mesh representation of buildings and roads, Appl. Acoust. 127 (2017) 297–304.

[11] J. Qi, L. Ding, S. Lim, Application of a decision-making framework for multi-objective optimisation of urban heat mitigation strategies, Urban Clim. 47 (2023) 101372.

[12] H. Qi, M. S. Altinakar, A GIS-based decision support system for integrated flood management under uncertainty with two dimensional numerical simulations, Environ. Model. Softw. 26 (2011) 817–821.

[13] J. Gaspari, K. Fabbri, M. Lucchi, The use of outdoor microclimate analysis to support decision making process: Case study of bufalini square in cesena, Sustain. Cities Soc. 42 (2018) 206–215.

[14] M. Taleghani, D. Sailor, G. A. Ban-Weiss, Micrometeorological simulations to predict the impacts of heat mitigation strategies on pedestrian thermal comfort in a los angeles neighborhood, Environ. Res. Lett. 11 (2016) 024003.

[15] T. Robineau, A. Rodler, B. Morille, D. Ramier, J. Sage, M. Musy, V. Graffin, E. Berthier, Coupling hydrological and microclimate models to simulate evapotranspiration from urban green areas and air temperature at the district scale, Urban Clim. 44 (2022) 101179.

[16] V. Giannico, M. Stafoggia, G. Spano, M. Elia, P. Dadvand, G. Sanesi, Characterizing green and gray space exposure for epidemiological studies: Moving from 2D to 3D indicators, Urban For. Urban Greening 72 (2022) 127567.

[17] J.-P. Virtanen, K. Jaalama, T. Puustinen, A. Julin, J. Hyyppä, H. Hyyppä, Near real-time semantic view analysis of 3D city models in web browser, ISPRS Int. J. Geoinf. 10 (2021) 138.

[18] Y. Qiang, S. Shen, Q. Chen, Visibility analysis of oceanic blue space using digital elevation models, Landsc. Urban Plan. 181 (2019) 92–102.

[19] B. Lei, R. Stouffs, F. Biljecki, Assessing and benchmarking 3D city models, Int. J. Geogr. Inf. Sci. 37 (2023) 788–809.

[20] B. Lei, P. Janssen, J. Stoter, F. Biljecki, Challenges of urban digital twins: A systematic review and a delphi expert survey, Autom. Constr. 147 (2023) 104716.

[21] I. Pađen, R. Peters, C. García-Sánchez, H. Ledoux, Automatic high-detailed building reconstruction workflow for urban microscale simulations, Build. Environ. 265 (2024) 111978.

[22] H. G. Kamath, M. Singh, N. Malviya, A. Martilli, L. He, D. Aliaga, C. He, F. Chen, L. A. Magruder, Z.-L. Yang, D. Niyogi, GLObal building heights for urban studies (UT-GLOBUS) for city- and street- scale urban simulations: Development and first applications, Sci. Data 11 (2024) 886.

[23] J. Tolan, H.-I. Yang, B. Nosarzewski, G. Couairon, H. V. Vo, J. Brandt, J. Spore, S. Majumdar, D. Haziza, J. Vamaraju, T. Moutakanni, P. Bojanowski, T. Johns, B. White, T. Tiecke, C. Couprie, Very high resolution canopy height maps from RGB imagery using self-supervised vision transformer and convolutional decoder trained on aerial lidar, Remote Sens. Environ. 300 (2024) 113888.

[24] D. Zanaga, R. Van De Kerchove, D. Daems, W. De Keersmaecker, C. Brockmann, G. Kirches, J. Wevers, O. Cartus, M. Santoro, S. Fritz, M. Lesiv, M. Herold, N.-E. Tsendbazar, P. Xu, F. Ramoino, O. Arino, ESA WorldCover 10 m 2021 v200, 2022.

[25] L. Hawker, P. Uhe, L. Paulo, J. Sosa, J. Savage, C. Sampson, J. Neal, A 30m global map of elevation with forests and buildings removed, Environ. Res. Lett. 17 (2022) 024016.

[26] W. Sirko, E. A. Brempong, J. T. C. Marcos, A. Annkah, A. Korme, M. A. Hassen, K. Sapkota, T. Shekel, A. Diack, S. Nevo, J. Hickey, J. Quinn, High-resolution building and road detection from sentinel-2, arXiv [cs.CV] (2023).

[27] H. Ledoux, F. Biljecki, B. Dukai, K. Kumar, R. Y. Peters, J. E. Stoter, T. J. F. Commandeur, 3dfier: automatic reconstruction of 3D city models, J. Open Source Softw. 6 (2021) 2866.

[28] F. Lindberg, C. S. B. Grimmond, A. Gabey, B. Huang, C. W. Kent, T. Sun, N. E. Theeuwes, L. Järvi, H. C. Ward, I. Capel-Timms, Y. Chang, P. Jonsson, N. Krave, D. Liu, D. Meyer, K. F. G. Olofson, J. Tan, D. Wästberg, L. Xue, Z. Zhang, Urban multi-scale environmental predictor (UMEP): An integrated tool for city-based climate services, Environ. Model. Softw. 99 (2018) 70–87.

[29] A. Katz, V. Sankaran, Mesh quality effects on the accuracy of CFD solutions on unstructured meshes, J. Comput. Phys. 230 (2011) 7670–7686.

[30] B. Willenborg, M. Pültz, T. H. Kolbe, Integration of semantic 3D city models and 3D mesh models for accuracy improvements of solar potential analyses, The International Archives of the Photogrammetry, Remote Sensing and Spatial Information Sciences 42 (2018) 223–230.

[31] J. Zhang, Y. Liu, B. Qin, D. Li, S. Yang, Q. Liu, A structured mesh generation tool for CFD simulations in process metallurgy, Metall. Mater. Trans. B 54 (2023) 481–486.

[32] J. Chen, J. Guo, C. Mou, Z. Xu, J. Wang, A structured mesh generation based on improved ray-tracing method for finite difference time domain simulation, Electronics (Basel) 13 (2024) 1189.

[33] A. Gargallo-Peiró, A. Folch, X. Roca, Representing urban geometries for unstructured mesh generation, Procedia Eng. 163 (2016) 175–185.

[34] D. Fisher-Gewirtzman, A. Shashkov, Y. Doytsher, Voxel based volumetric visibility analysis of urban environments, Surv. Rev. 45 (2013) 451–461.

[35] M. Aleksandrov, S. Zlatanova, L. Kimmel, J. Barton, B. Gorte, Voxel-based visibility analysis for safety assessment of urban environments, ISPRS Ann. Photogramm. Remote Sens. Spat. Inf. Sci. IV-4/W8 (2019) 11–17.

[36] B. Gorte, S. Zlatanova, M. Pilouk, A. Diakite, J. Barton, 3D data integration in the voxel domain, ISPRS Ann. Photogramm. Remote Sens. Spat. Inf. Sci. X-4-2024 (2024) 133–140.

[37] J. Xiao, T. Yuizono, Climate-adaptive landscape design: Microclimate and thermal comfort regulation of station square in the hokuriku region, japan, Build. Environ. 212 (2022) 108813.

[38] Y. Li, W. Ouyang, S. Yin, Z. Tan, C. Ren, Microclimate and its influencing factors in residential public spaces during heat waves: An empirical study in hong kong, Build. Environ. 236 (2023) 110225.

[39] M. Taleghani, A. Marshall, R. Fitton, W. Swan, Renaturing a microclimate: The impact of greening a neighbourhood on indoor thermal comfort during a heatwave in manchester, UK, Solar Energy 182 (2019) 245–255.

[40] I. Kousis, M. Manni, A. L. Pisello, Environmental mobile monitoring of urban microclimates: A review, Renewable Sustainable Energy Rev. 169 (2022) 112847.

[41] G. Chen, L. Rong, G. Zhang, Unsteady-state CFD simulations on the impacts of urban geometry on outdoor thermal comfort within idealized building arrays, Sustain. Cities Soc. 74 (2021) 103187.

[42] F. Kong, J. Chen, A. Middel, H. Yin, M. Li, T. Sun, N. Zhang, J. Huang, H. Liu, K. Zhou, J. Ma, Impact of 3-D urban landscape patterns on the outdoor thermal environment: A modelling study with SOLWEIG, Comput. Environ. Urban Syst. 94 (2022) 101773.

[43] X. Li, G. Wang, Examining runner's outdoor heat exposure using urban microclimate modeling and GPS trajectory mining, Comput. Environ. Urban Syst. 89 (2021) 101678.

[44] A. Forouzandeh, Prediction of surface temperature of building surrounding envelopes using holistic microclimate ENVI-met model, Sustain. Cities Soc. 70 (2021) 102878.

[45] L. Malys, M. Musy, C. Inard, Microclimate and building energy consumption: study of different coupling methods, Adv. Build. Energy Res. 9 (2015) 151–174.

[46] N. Sezer, H. Yoonus, D. Zhan, L. l. Wang, I. G. Hassan, M. A. Rahman, Urban microclimate and building energy models: A review of the latest progress in coupling strategies, Renew. Sustain. Energy Rev. 184 (2023) 113577.

[47] R. Kadaverugu, A. Sharma, C. Matli, R. Biniwale, High resolution urban air quality modeling by coupling CFD and mesoscale models: A review, Asia Pac. J. Atmos. Sci. 55 (2019) 539–556.

[48] K.-H. Kwak, J.-J. Baik, Y.-H. Ryu, S.-H. Lee, Urban air quality simulation in a high-rise building area using a CFD model coupled with mesoscale meteorological and chemistry-transport models, Atmos. Environ. (1994) 100 (2015) 167–177.

[49] B. Blocken, W. D. Janssen, T. van Hooff, CFD simulation for pedestrian wind comfort and wind safety in urban areas: General decision framework and case study for the eindhoven university campus, Environ. Model. Softw. 30 (2012) 15–34.

[50] B. Blocken, T. Stathopoulos, J. P. A. J. van Beeck, Pedestrian-level wind conditions around buildings: Review of wind-tunnel and CFD techniques and their accuracy for wind comfort assessment, Build. Environ. 100 (2016) 50–81.

[51] B. Mou, B.-J. He, D.-X. Zhao, K.-W. Chau, Numerical simulation of the effects of building dimensional variation on wind pressure distribution, Eng. Appl. Comput. Fluid Mech. 11 (2017) 293–309.

[52] T. Stathopoulos, B. A. Baskaran, Computer simulation of wind environmental conditions around buildings, Eng. Struct. 18 (1996) 876–885.

[53] R. H. Grant, G. M. Heisler, W. Gao, Estimation of pedestrian level UV exposure under trees, Photochem. Photobiol. 75 (2002) 369–376.

[54] O. M. Galal, H. Mahmoud, D. Sailor, Impact of evolving building morphology on microclimate in a hot arid climate, Sustain. Cities Soc. 54 (2020) 102011.

[55] J. Zhang, Z. Li, Y. Wei, D. Hu, The impact of the building morphology on microclimate and thermal comfort-a case study in beijing, Build. Environ. 223 (2022) 109469.

[56] B. Hong, B. Lin, Numerical studies of the outdoor wind environment and thermal comfort at pedestrian level in housing blocks with different building layout patterns and trees arrangement, Renew. Energy 73 (2015) 18–27.

[57] Z. Wu, P. Dou, L. Chen, Comparative and combinative cooling effects of different spatial arrangements of buildings and trees on microclimate, Sustain. Cities Soc. 51 (2019) 101711.

[58] T. E. Morakinyo, Y. F. Lam, Simulation study on the impact of tree-configuration, planting pattern and wind condition on street-canyon's micro-climate and thermal comfort, Build. Environ. 103 (2016) 262–275.

[59] R. Li, F. Zeng, Y. Zhao, Y. Wu, J. Niu, L. l. Wang, N. Gao, X. Shi, CFD simulations of the tree effect on the outdoor microclimate by coupling the canopy energy balance model, Build. Environ. 230 (2023) 109995.

[60] Y. Wang, F. Bakker, R. de Groot, H. Wortche, R. Leemans, Effects of urban trees on local outdoor microclimate: synthesizing field measurements by numerical modelling, Urban Ecosyst. 18 (2015) 1305–1331.

[61] H. Oshio, T. Kiyono, T. Asawa, Numerical simulation of the nocturnal cooling effect of urban trees considering the leaf area density distribution, Urban For. Urban Greening 66 (2021) 127391.

[62] R. Li, Y. Zhao, M. Chang, F. Zeng, Y. Wu, L. l. Wang, J. Niu, X. Shi, N. Gao, Numerical simulation methods of tree effects on microclimate: A review, Renew. Sustain. Energy Rev. 205 (2024) 114852.

[63] Y. He, E. S. Lin, W. Zhang, C. L. Tan, P. Y. Tan, N. H. Wong, Local microclimate above shrub and grass in tropical city: A case study in singapore, Urban Clim. 43 (2022) 101142.

[64] X. Yang, L. Zhao, M. Bruse, Q. Meng, Evaluation of a microclimate model for predicting the thermal behavior of different ground surfaces, Build. Environ. 60 (2013) 93–104.

[65] X. Wang, P. Liu, G. Xu, Influence of grass lawns on the summer thermal environment and microclimate of heritage sites: a case study of fuling mausoleum, china, Herit. Sci. 9 (2021).

[66] M. Robitu, M. Musy, C. Inard, D. Groleau, Modeling the influence of vegetation and water pond on urban microclimate, Sol. Energy 80 (2006) 435–447.

[67] H. Du, Y. Cai, F. Zhou, H. Jiang, W. Jiang, Y. Xu, Urban blue-green space planning based on thermal environment simulation: A case study of shanghai, china, Ecol. Indic. 106 (2019) 105501.

[68] N. Imam Syafii, M. Ichinose, E. Kumakura, S. K. Jusuf, K. Chigusa, N. H. Wong, Thermal environment assessment around bodies of water in urban canyons: A scale model study, Sustain. Cities Soc. 34 (2017) 79–89.

[69] L. Sun, A. Nottrott, J. Kleissl, Effect of hilly urban morphology on dispersion in the urban boundary layer, Build. Environ. 48 (2012) 195–205.

[70] F. Abd-Alhamid, M. Kent, Y. Wu, Quantifying window view quality: A review on view perception assessment and representation methods, Build. Environ. 227 (2023) 109742.

[71] S. Yu, B. Yu, W. Song, B. Wu, J. Zhou, Y. Huang, J. Wu, F. Zhao, W. Mao, View-based greenery: A three-dimensional assessment of city buildings' green visibility using floor green view index, Landsc. Urban Plan. 152 (2016) 13–26.

[72] Y. K. Yi, H. Kim, Universal visible sky factor: A method for calculating the three-dimensional visible sky ratio, Build. Environ. 123 (2017) 390–403.

[73] K. Fujiwara, T. Asawa, T. Kiyono, Multi-objective optimization for tree arrangement in urban open space considering thermal radiant environment and scenery, AIJ J. Technol. Des. 28 (2022) 320–325.

[74] S. M. Labib, J. J. Huck, S. Lindley, Modelling and mapping eye-level greenness visibility exposure using multi-source data at high spatial resolutions, Sci. Total Environ. 755 (2021) 143050.

[75] F. Biljecki, T. Zhao, X. Liang, Y. Hou, Sensitivity of measuring the urban form and greenery using street-level imagery: A comparative study of approaches and visual perspectives, Int. J. Appl. Earth Obs. Geoinf. 122 (2023) 103385.

[76] D. Ki, S. Lee, Analyzing the effects of green view index of neighborhood streets on walking time using google street view and deep learning, Landsc. Urban Plan. 205 (2021) 103920.

[77] W. Zhang, H. Zeng, Spatial differentiation characteristics and influencing factors of the green view index in urban areas based on street view images: A case study of futian district, shenzhen, china, Urban For. Urban Greening 93 (2024) 128219.

[78] X. Liang, T. Zhao, F. Biljecki, Revealing spatio-temporal evolution of urban visual environments with street view imagery, Landsc. Urban Plan. 237 (2023) 104802.

[79] K. Ito, Y. Zhu, M. Abdelrahman, X. Liang, Z. Fan, Y. Hou, T. Zhao, R. Ma, K. Fujiwara, J. Ouyang, M. Quintana, F. Biljecki, ZenSVI: An open-source software for the integrated acquisition, processing and analysis of street view imagery towards scalable urban science, Comput. Environ. Urban Syst. 119 (2025) 102283.

[80] Y. Lu, C. Sarkar, Y. Xiao, The effect of street-level greenery on walking behavior: Evidence from hong kong, Soc. Sci. Med. 208 (2018) 41–49.

[81] K. Ito, F. Biljecki, Assessing bikeability with street view imagery and computer vision, Transp. Res. Part C: Emerg. Technol. 132 (2021) 103371.

[82] R. Wang, B. Yang, Y. Yao, M. S. Bloom, Z. Feng, Y. Yuan, J. Zhang, P. Liu, W. Wu, Y. Lu, G. Baranyi, R. Wu, Y. Liu, G. Dong, Residential greenness, air pollution and psychological well-being among urban residents in guangzhou, china, Sci. Total Environ. 711 (2020) 134843.

[83] C. Wu, Y. Du, S. Li, P. Liu, X. Ye, Does visual contact with green space impact housing prices? an integrated approach of machine learning and hedonic modeling based on the perception of green space, Land Use Policy 115 (2022) 106048.

[84] J. Yang, H. Rong, Y. Kang, F. Zhang, A. Chegut, The financial impact of street-level greenery on new york commercial buildings, Landsc. Urban Plan. 214 (2021) 104162.

[85] J. Luo, T. Zhao, L. Cao, F. Biljecki, Water view imagery: Perception and evaluation of urban waterscapes worldwide, Ecol. Indic. 145 (2022) 109615.

[86] Y. Wang, Z. He, W. Zhai, S. Wang, C. Zhao, How do the 3D urban morphological characteristics spatiotemporally affect the urban thermal environment? a case study of san antonio, Build. Environ. 261 (2024) 111738.

[87] R. Peters, B. Dukai, S. Vitalis, J. van Liempt, J. Stoter, Automated 3D reconstruction of LoD2 and LoD1 models for all 10 million buildings of the netherlands, Photogramm. Eng. Remote Sensing 88 (2022) 165–170.

[88] Y. Rong, T. Zhang, Y. Zheng, C. Hu, L. Peng, P. Feng, Three-dimensional urban flood inundation simulation based on digital aerial photogrammetry, J. Hydrol. (Amst.) 584 (2020) 124308.

[89] R. Matsuoka, T. Takemoto, G. Takahashi, T. Inazawa, S. Sogo, Estimation of photovoltaic potential of urban buildings considering a solar panel arrangement using a 3D city model, ISPRS Ann. Photogramm. Remote Sens. Spat. Inf. Sci. X-4/W4-2024 (2024) 123–130.

[90] X. Zhang, F. Ludwig, Shade for pedestrians: A novel approach to calculate the spatio-temporal shade benefits of street trees considering pedestrian flow, Build. Environ. 272 (2025) 112662.

[91] R. Nouvel, A. Mastrucci, U. Leopold, O. Baume, V. Coors, U. Eicker, Combining GIS-based statistical and engineering urban heat consumption models: Towards a new framework for multi-scale policy support, Energy Build. 107 (2015) 204–212.

[92] H. Harter, B. Willenborg, W. Lang, T. H. Kolbe, Climate-neutral municipal building stock - life cycle assessment of large residential building stocks based on semantic 3D city models, Energy Build. 292 (2023) 113141.

[93] A. Malhotra, M. Shamovich, J. Frisch, C. van Treeck, Urban energy simulations using open CityGML models: A comparative analysis, Energy Build. 255 (2022) 111658.

[94] T. G. Farr, M. Kobrick, Shuttle radar topography mission produces a wealth of data, Eos, Transactions American Geophysical Union 81 (2000) 583–585.

[95] X. Ding, Y. Zhao, D. Strebel, Y. Fan, J. Ge, J. Carmeliet, A WRF-UCM-SOLWEIG framework for mapping thermal comfort and quantifying urban climate drivers: Advancing spatial and temporal resolutions at city scale, Sustain. Cities Soc. 112 (2024) 105628.

[96] W. Yap, R. Stouffs, F. Biljecki, Urbanity: automated modelling and analysis of multidimensional networks in cities, npj Urban Sustainability 3 (2023) 1–11.

[97] M. Gholami, A. Middel, D. Torreggiani, P. Tassinari, A. Barbaresi, A hybrid python approach to assess microscale human thermal stress in urban environments, Build. Environ. 248 (2024) 111054.

[98] S. Balakrishnan, B. Cassottana, InfraRisk: An open-source simulation platform for resilience analysis in interconnected power–water–transport networks, Sustain. Cities Soc. 83 (2022) 103963.

[99] G. Boeing, OSMnx: New methods for acquiring, constructing, analyzing, and visualizing complex street networks, Comput. Environ. Urban Syst. 65 (2017) 126–139.

[100] H. Martin, Y. Hong, N. Wiedemann, D. Bucher, M. Raubal, Trackintel: An open-source python library for human mobility analysis, Comput. Environ. Urban Syst. 101 (2023) 101938.

[101] S. Huttner, Further development and application of the 3D microclimate simulation ENVI-met, Ph.D. thesis, Mainz, Univ., Diss., 2012, 2012.

[102] Z. Liu, S. Zhang, X. Shao, Z. Wu, Accurate and efficient urban wind prediction at city-scale with memory-scalable graph neural network, Sustain. Cities Soc. 99 (2023) 104935.

[103] B. Maronga, S. Banzhaf, C. Burmeister, T. Esch, R. Forkel, D. Fröhlich, V. Fuka, K. F. Gehrke, J. Geletič, S. Giersch, T. Gronemeier, G. Groß, W. Heldens, A. Hellsten, F. Hoffmann, A. Inagaki, E. Kadasch, F. Kanani-Sühring, K. Ketelsen, B. A. Khan, C. Knigge, H. Knoop, P. Krč, M. Kurppa, H. Maamari, A. Matzarakis, M. Mauder, M. Pallasch, D. Pavlik, J. Pfafferott, J. Resler, S. Rissmann, E. Russo, M. Salim, M. Schrempf, J. Schwenkel, G. Seckmeyer, S. Schubert, M. Sühring, R. von Tils, L. Vollmer, S. Ward, B. Witha, H. Wurps, J. Zeidler, S. Raasch, Overview of the PALM model system 6.0, Geosci. Model Dev. 13 (2020) 1335–1372.

[104] N. Milojevic-Dupont, F. Wagner, F. Nachtigall, J. Hu, G. B. Brüser, M. Zumwald, F. Biljecki, N. Heeren, L. H. Kaack, P.-P. Pichler, F. Creutzig, EUBUCCO v0.1: European building stock characteristics in a common and open database for 200+ million individual buildings, Sci Data 10 (2023) 147.

[105] Microsoft, Microsoft building footprints, 2024. URL: `https://github.com/microsoft/GlobalMLBuildingFootprints/`, accessed: 2024-11-14.

[106] B. Herfort, S. Lautenbach, J. Porto de Albuquerque, J. Anderson, A. Zipf, A spatio-temporal analysis investigating completeness and inequalities of global urban building data in OpenStreetMap, Nat. Commun. 14 (2023) 3985.

[107] F. Biljecki, Y. S. Chow, K. Lee, Quality of crowdsourced geospatial building information: A global assessment of OpenStreetMap attributes, Building and Environment 237 (2023) 110295.

[108] K. Van Tricht, J. Degerickx, S. Gilliams, D. Zanaga, M. Battude, A. Grosu, J. Brombacher, M. Lesiv, J. C. L. Bayas, S. Karanam, S. Fritz, I. Becker-Reshef, B. Franch, B. Mollà-Bononad, H. Boogaard, A. K. Pratihast, B. Koetz, Z. Szantoi, WorldCereal: a dynamic open-source system for global-scale, seasonal, and reproducible crop and irrigation mapping, Earth Syst. Sci. Data 15 (2023) 5491–5515.

[109] M. Shimada, T. Itoh, T. Motooka, M. Watanabe, T. Shiraishi, R. Thapa, R. Lucas, New global forest/non-forest maps from ALOS PALSAR data (2007–2010), Remote Sens. Environ. 155 (2014) 13–31.

[110] GLIMS Consortium, Glims glacier database, 2005. URL: `https://doi.org/10.7265/N5V98602`, nSIDC-0272, Version 1.

[111] B. H. Raup, A. Racoviteanu, S. J. Khalsa, C. Helm, R. Armstrong, Y. Arnaud, The glims geospatial glacier database: A new tool for studying glacier change, Global and Planetary Change 56 (2007).

[112] K. Karra, C. Kontgis, Z. Statman-Weil, J. C. Mazzariello, M. Mathis, S. P. Brumby, Global land use / land cover with sentinel 2 and deep learning, in: 2021 IEEE International Geoscience and Remote Sensing Symposium IGARSS, IEEE, 2021, pp. 4704–4707.

[113] C. F. Brown, S. P. Brumby, B. Guzder-Williams, T. Birch, S. B. Hyde, J. Mazzariello, W. Czerwinski, V. J. Pasquarella, R. Haertel, S. Ilyushchenko, K. Schwehr, M. Weisse, F. Stolle, C. Hanson, O. Guinan, R. Moore, A. M. Tait, Dynamic world, near real-time global 10 m land use land cover mapping, Sci. Data 9 (2022) 251.

[114] N. Yokoya, J. Xia, C. Broni-Bediako, Submeter-level land cover mapping of japan, Int. J. Appl. Earth Obs. Geoinf. 127 (2024) 103660.

[115] Y. Zhang, G. Chen, S. W. Myint, Y. Zhou, G. J. Hay, J. Vukomanovic, R. K. Meentemeyer, UrbanWatch: A 1-meter resolution land cover and land use database for 22 major cities in the united states, Remote Sens. Environ. 278 (2022) 113106.

[116] P. Potapov, X. Li, A. Hernandez-Serna, A. Tyukavina, M. C. Hansen, A. Kommareddy, A. Pickens, S. Turubanova, H. Tang, C. E. Silva, J. Armston, R. Dubayah, J. B. Blair, M. Hofton, Mapping global forest canopy height through integration of GEDI and landsat data, Remote Sens. Environ. 253 (2021) 112165.

[117] M. Simard, L. Fatoyinbo, C. Smetanka, V. H. Rivera-Monroy, E. Castañeda-Moya, N. Thomas, T. Van der Stocken, Mangrove canopy height globally related to precipitation, temperature and cyclone frequency, Nat. Geosci. 12 (2019) 40–45.

[118] B. Ma, R. J. Hauer, J. Östberg, A. K. Koeser, H. Wei, C. Xu, A global basis of urban tree inventories: What comes first the inventory or the program, Urban For. Urban Greening 60 (2021) 127087.

[119] A. B. Nielsen, J. Östberg, T. Delshammar, Review of urban tree inventory methods used to collect data at single-tree level, Arboriculture & Urban Forestry (AUF) 40 (2014) 96–111.

[120] A. Ossola, M. J. Hoeppner, H. M. Burley, R. V. Gallagher, L. J. Beaumont, M. R. Leishman, The global urban tree inventory: A database of the diverse tree flora that inhabits the world's cities, Glob. Ecol. Biogeogr. 29 (2020) 1907–1914.

[121] Direction des Espaces Verts et de l'Environnement - Ville de Paris, Arbres, 2024. URL: https://opendata.paris.fr/explore/dataset/les-arbres/information/, accessed: 2024-11-14.

[122] Gerència d'Àrea Agenda 2030, Transició Digital i Esports, Local interest trees from barcelona, 2024. URL: https://opendata-ajuntament.barcelona.cat/data/es/dataset/arbres-interes-local, accessed: 2024-11-14.

[123] Department of Parks and Recreation (DPR), 2015 street tree census - tree data, 2024. URL: https://data.cityofnewyork.us/Environment/2015-Street-Tree-Census-Tree-Data/uvpi-gqnh/about_data, accessed: 2024-11-14.

[124] N. Lang, W. Jetz, K. Schindler, J. D. Wegner, A high-resolution canopy height model of the earth, Nat Ecol Evol (2023).

[125] NASA JPL, NASADEM Merged DEM Global 1 arc second V001, 2020. doi:10.5067/MEaSUREs/NASADEM/NASADEM_HGT.001, accessed 2024-10-28.

[126] European Space Agency, Copernicus global digital elevation model, 2024. Accessed: 2024-11-13.

[127] T. Tadono, H. Ishida, F. Oda, S. Naito, K. Minakawa, H. Iwamoto, Precise global DEM generation by ALOS PRISM, ISPRS Ann. Photogramm. Remote Sens. Spat. Inf. Sci. II-4 (2014) 71–76.

[128] F. E. O'Loughlin, R. C. D. Paiva, M. Durand, D. E. Alsdorf, P. D. Bates, A multi-sensor approach towards a global vegetation corrected SRTM DEM product, Remote Sens. Environ. 182 (2016) 49–59.

[129] M. Pronk, A. Hooijer, D. Eilander, A. Haag, T. de Jong, M. Vousdoukas, R. Vernimmen, H. Ledoux, M. Eleveld, DeltaDTM: A global coastal digital terrain model, Sci. Data 11 (2024) 273.

[130] U.S. Geological Survey, 1 meter digital elevation models (dems) - usgs national map 3dep downloadable data collection, 2023. URL: https://data.usgs.gov/datacatalog/data/USGS:77ae0551-c61e-4979-aedd-d797abdcde0e, accessed: 2024-11-13.

[131] Environment Agency, Lidar composite digital terrain model (dtm) - 1m, 2024. URL: https://environment.data.gov.uk/dataset/13787b9a-26a4-4775-8523-806d13af58fc, accessed: 2024-11-13.

[132] Geoscience Australia, Digital elevation model (dem) of australia derived from lidar 5 metre grid, 2015. Accessed: 2024-11-13.

[133] National Institute of Geographic and Forest Information, Rge alti® 1m, 2024. URL: https://geoservices.ign.fr/rgealti, accessed: 2024-11-13.

[134] J. Liang, J. Gong, A sparse voxel octree-based framework for computing solar radiation using 3D city models, ISPRS Int. J. Geoinf. 6 (2017) 106.

[135] Y. Park, J.-M. Guldmann, D. Liu, Impacts of tree and building shades on the urban heat island: Combining remote sensing, 3D digital city and spatial regression approaches, Comput. Environ. Urban Syst. 88 (2021) 101655.

[136] K.-T. Huang, S.-R. Yang, A. Matzarakis, T.-P. Lin, Identifying outdoor thermal risk areas and evaluation of future thermal comfort concerning shading orientation in a traditional settlement, Sci. Total Environ. 626 (2018) 567–580.

[137] S. Coccolo, J. Kämpf, J.-L. Scartezzini, D. Pearlmutter, Outdoor human comfort and thermal stress: A comprehensive review on models and standards, Urban Climate 18 (2016) 33–57.

[138] A. Palliwal, S. Song, H. T. W. Tan, F. Biljecki, 3D city models for urban farming site identification in buildings, Comput. Environ. Urban Syst. 86 (2021) 101584.

[139] J. Hofierka, J. Kaňuk, Assessment of photovoltaic potential in urban areas using open-source solar radiation tools, Renewable Energy 34 (2009) 2206–2214.

[140] J. D. Mondol, Y. G. Yohanis, B. Norton, Solar radiation modelling for the simulation of photovoltaic systems, Renewable Energy 33 (2008) 1109–1120.

[141] J. C. Lam, D. H. W. Li, An analysis of daylighting and solar heat for cooling-dominated office buildings, Sol. Energy 65 (1999) 251–262.

[142] F. Causone, S. P. Corgnati, M. Filippi, B. W. Olesen, Solar radiation and cooling load calculation for radiant systems: Definition and evaluation of the direct solar load, Energy Build. 42 (2010) 305–314.

[143] F. Pružinec, R. Ďuračiová, A point-cloud solar radiation tool, Energies 15 (2022) 7018.

[144] M. Monsi, T. Saeki, On the factor light in plant communities and its importance for matter production. 1953, Ann. Bot. 95 (2004) 549–567.

[145] M. Mor, D. Fisher-Gewirtzman, R. Yosifof, S. Dalyot, 3D visibility analysis for evaluating the attractiveness of tourism routes computed from social media photos, ISPRS Int. J. Geoinf. 10 (2021) 275.

[146] R. Wróżyński, K. Pyszny, M. Wróżyńska, Reaching beyond GIS for comprehensive 3D visibility analysis, Landsc. Urban Plan. 247 (2024) 105074.

[147] G. Filomena, J. A. Verstegen, Modelling the effect of landmarks on pedestrian dynamics in urban environments, Computers, Environment and Urban Systems 86 (2021) 101573. doi:10.1016/j.compenvurbsys.2020.101573.

[148] D. Yesiltepe, R. Conroy Dalton, A. Ozbil Torun, Landmarks in wayfinding: a review of the existing literature, Cognitive Processing 22 (2021) 369–410. doi:10.1007/s10339-021-01012-x.

[149] L. Sabesan, L. Meetiyagoda, S. Rathnasekara, Landmarks and walkability: wayfinding during nighttime in a tourism-based city. case study of jaffna, sri lanka, GeoJournal 89 (2024) 1–15.

[150] G. Yuan, W. Yuyao, Y. Miao, Selecting building height control indicators of landmark skylines: A visual perception experiment, Environ. Plan. B Urban Anal. City Sci. (2024).

[151] I. Turan, A. Chegut, D. Fink, C. Reinhart, Development of view potential metrics and the financial impact of views on office rents, Landscape and Urban Planning 215 (2021) 104193. doi:10.1016/j.landurbplan.2021.104193.

[152] Z. Liu, W. Cheng, C. Y. Jim, T. E. Morakinyo, Y. Shi, E. Ng, Heat mitigation benefits of urban green and blue infrastructures: A systematic review of modeling techniques, validation and scenario simulation in ENVI-met V4, Build. Environ. 200 (2021) 107939.

[153] W. Ouyang, T. Sinsel, H. Simon, T. E. Morakinyo, H. Liu, E. Ng, Evaluating the thermal-radiative performance of ENVI-met model for green infrastructure typologies: Experience from a subtropical climate, Build. Environ. 207 (2022) 108427.

[154] C. R. Harris, K. J. Millman, S. J. van der Walt, R. Gommers, P. Virtanen, D. Cournapeau, E. Wieser, J. Taylor, S. Berg, N. J. Smith, R. Kern, M. Picus, S. Hoyer, M. H. van Kerkwijk, M. Brett, A. Haldane, J. F. del Río, M. Wiebe, P. Peterson, P. Gérard-Marchant, K. Sheppard, T. Reddy, W. Weckesser, H. Abbasi, C. Gohlke, T. E. Oliphant, Array programming with NumPy, Nature 585 (2020) 357–362.

[155] P. Bröde, D. Fiala, K. Błażejczyk, I. Holmér, G. Jendritzky, B. Kampmann, B. Tinz, G. Havenith, Deriving the operational procedure for the universal thermal climate index (UTCI), Int. J. Biometeorol. 56 (2012) 481–494.

[156] X. Yang, L. Zhao, M. Bruse, Q. Meng, Evaluation of a microclimate model for predicting the thermal behavior of different ground surfaces, Building and Environment 60 (2013) 93–104. doi:10.1016/j.buildenv.2012.11.008.

[157] S. Tsoka, A. Tsikaloudaki, T. Theodosiou, Analyzing the ENVI-met microclimate model's performance and assessing cool materials and urban vegetation applications–A review, Sustainable Cities and Society 43 (2018) 55–76. doi:10.1016/j.scs.2018.08.009.

[158] Z. Liu, W. Cheng, C. Jim, T. E. Morakinyo, Y. Shi, E. Ng, Heat mitigation benefits of urban green and blue infrastructures: A systematic review of modeling techniques, validation and scenario simulation in ENVI-met V4, Building and Environment 200 (2021) 107939. doi:10.1016/j.buildenv.2021.107939.

[159] F. Biljecki, K. Arroyo Ohori, Automatic Semantic-preserving Conversion Between OBJ and CityGML, in: Eurographics Workshop on Urban Data Modelling and Visualisation 2015, Delft, Netherlands, 2015, pp. 25–30.

[160] H. Ledoux, K. Arroyo Ohori, K. Kumar, B. Dukai, A. Labetski, S. Vitalis, Cityjson: A compact and easy-to-use encoding of the citygml data model, Open Geospatial Data, Software and Standards 4 (2019) 1–12.

[161] S. Vitalis, A. Labetski, F. Boersma, F. Dahle, X. Li, K. Arroyo Ohori, H. Ledoux, J. Stoter, Cityjson+ web= ninja, ISPRS Annals of the Photogrammetry, Remote Sensing and Spatial Information Sciences 6 (2020) 167–173.

[162] D. Petrova-Antonova, S. Malinov, L. Mrosla, A. Petrov, Towards a conceptual model of citygml 3.0 vegetation ade, The International Archives of the Photogrammetry, Remote Sensing and Spatial Information Sciences 48 (2024) 155–161.

[163] B. Lei, X. Liang, F. Biljecki, Integrating human perception in 3d city models and urban digital twins, ISPRS Annals of the Photogrammetry, Remote Sensing and Spatial Information Sciences 10 (2024) 211–218.

[164] C. Marino, A. Nucara, M. Pietrafesa, Does window-to-wall ratio have a significant effect on the energy consumption of buildings? a parametric analysis in italian climate conditions, Journal of Building Engineering 13 (2017) 169–183.

[165] L. Troup, R. Phillips, M. J. Eckelman, D. Fannon, Effect of window-to-wall ratio on measured energy consumption in US office buildings, Energy and Buildings 203 (2019) 109434.

[166] F. Chi, Y. Wang, R. Wang, G. Li, C. Peng, An investigation of optimal window-to-wall ratio based on changes in building orientations for traditional dwellings, Solar Energy 195 (2020) 64–81.

[167] X. Liang, J. Xie, T. Zhao, R. Stouffs, F. Biljecki, Openfacades: An open framework for architectural caption and attribute data enrichment via street view imagery, 2025. URL: https://arxiv.org/abs/2504.02866. arXiv:2504.02866.

[168] J. Kang, M. Körner, Y. Wang, H. Taubenböck, X. X. Zhu, Building instance classification using street view images, ISPRS Journal of Photogrammetry and Remote Sensing 145 (2018) 44–59.

[169] M. Sun, F. Zhang, F. Duarte, C. Ratti, Understanding architecture age and style through deep learning, Cities 128 (2022) 103787.

[170] D. Raghu, M. J. J. Bucher, C. De Wolf, Towards a 'resource cadastre' for a circular economy – Urban-scale building material detection using street view imagery and computer vision, Resources, Conservation and Recycling 198 (2023) 107140.

[171] K. Fabbri, J. Gaspari, S. Bartoletti, E. Antonini, Effect of facade reflectance on outdoor microclimate: An italian case study, Sustainable cities and society 54 (2020) 101984.

[172] V. Harish, A. Kumar, A review on modeling and simulation of building energy systems, Renewable and sustainable energy reviews 56 (2016) 1272–1292.

[173] T. Ren, S. Liu, A. Zeng, J. Lin, K. Li, H. Cao, J. Chen, X. Huang, Y. Chen, F. Yan, Z. Zeng, H. Zhang, F. Li, J. Yang, H. Li, Q. Jiang, L. Zhang, Grounded SAM: Assembling open-world models for diverse visual tasks, 2024. URL: http://arxiv.org/abs/2401.14159. arXiv:2401.14159 [cs].

[174] K. Fath, J. Stengel, W. Sprenger, H. R. Wilson, F. Schultmann, T. E. Kuhn, A method for predicting the economic potential of (building-integrated) photovoltaics in urban areas based on hourly radiance simulations, Sol. Energy 116 (2015) 357–370.